Applied Thermal Engineering 261 (2025) 125073

Contents lists available at ScienceDirect

Applied Thermal Engineering

journal homepage: www.elsevier.com/locate/apthermeng

Research Paper

# Effect of different chamber geometries on combustion formation to reduce harmful emissions

Arun Teja Doppalapudi [a,*], Abul Kalam Azad [a], Mohammad Masud Kamal Khan [b], Aman Maung Than Oo [c]

[a] School of Engineering and Technology, Central Queensland University, 120 Spencer Street, Melbourne, VIC 3000, Australia
[b] School of Engineering, Computer & Mathematical Sciences, Auckland University of Technology, Auckland, New Zealand
[c] School of Engineering, Macquarie University, Sydney, New South Wales, Australia

ARTICLE INFO

*Keywords:*
Combustion simulation
Diesel engine
$NO_x$ emissions
Combustion chamber
Combustion behaviour
CFD simulation

ABSTRACT

The combustion process in internal combustion engines is the primary aspect of engine performance and emissions. Combustion chamber geometries such as grooved combustion chamber (GCC), shallow depth combustion chamber (SCC), and bathtub combustion chamber (BTCC) are used to investigate the effect of combustion rates on the emission parameters with respect to the standard flat combustion chamber (FCC). The impact of chamber modifications was simulated with an IC engine model using advanced chemical kinetics. Combustion parameters such as in-cylinder temperature, turbulence, and heat release rates were observed. The validated computational model assisted in analyzing combustion formations and their correlation with emissions like mass fractions, CO, $CO_2$, and $NO_x$. The results revealed that the modified chambers avoided the formation of fuel pockets and improved combustion behaviour compared to FCC. At 440 $^oCA$, peak $NO_x$ emissions were higher by 14.95%, 27.10%, and 15.89% for GCC, SCC, and BTCC chambers, respectively, compared to the FCC chamber. At 440 $^oCA$, $CO_2$ emissions increased by 2.22%, 2.78%, and 2.78% for GCC, SCC, and BTCC chambers, respectively, compared to the FCC. The GCC chamber's geometry influences the air–fuel mixture distribution, leading to stratified combustion zones and utilizing both bowl and squish regions. The study concludes that GCC chambers can significantly enhance efficiency and reduce emissions by influencing temperature profiles and mass fraction distributions. The study recommends using the GCC chamber with optimized injection profiles for better combustion and improved swirl rates.

## 1. Introduction

Internal combustion (IC) engines majorly contribute to greenhouse gas emissions. For instance, in 2022, global carbon dioxide ($CO_2$) emissions from the transport sector increased by over 250 million tonnes, reaching almost eight gigatons of $CO_2$, which is a 3 % rise compared to 2021 [1]. Several advanced technologies are implemented to reduce emissions from these engines. Techniques such as fuel modifications, combustion process modifications, and exhaust gas aftertreatment systems have significantly reduced emissions from IC engines [2]. Among these, combustion process modifications have proved to be an excellent active technique directly correlating with the combustion rate [3]. From an economic point of view, changes to the combustion chamber geometries offer minimal engine modification and perform better combustion with reduced emissions [4]. Moreover, chamber modifications offer better air–fuel mixing and complete combustion with alternative fuels such as biodiesel [5], alcohols [6], natural gas [7] and hydrogen fuels [8,9].

Chamber modifications have improved control over combustion formation and distribution [10]. Modifying the combustion chamber volume can tune the fuel distribution and enhance the combustion occurrence rates inside the chamber [11]. Piston bowl modifications guide the air–fuel into the bowl chamber and perform combustion in a small radius region (piston-bowl) compared to the large cylinder bore. Chamber modifications have shown reduced specific fuel consumption, increased engine performance, and reduced carbon monoxide (CO), hydrocarbon (HC), soot, and smoke emissions [12]. Despite this, chamber modifications still face the problems of high turbulence formation and higher nitrogen oxide ($NO_x$) emissions. For instance, Gulcan and Ciniviz [13] observed a decrease in smoke, HC, and CO emissions by an average of 18 %, 10 %, and 3 % and an increase in nitric oxide (NO)

* Corresponding author.
*E-mail addresses:* a.doppalapudi@cqu.edu.au (A.T. Doppalapudi), a.k.azad@cqu.edu.au (A.K. Azad).

https://doi.org/10.1016/j.applthermaleng.2024.125073
Received 5 August 2024; Received in revised form 29 October 2024; Accepted 25 November 2024
Available online 4 December 2024

**Nomenclature**

| Symbol | Meaning |
|---|---|
| $\rho$ | Density |
| $\vec{v}$ | Velocity |
| $\vec{r}$ | Radial distance |
| $C_d$ | Discharge Coefficient |
| $D$ | Diffusion coefficient |
| $G_k$ | Generation of turbulence kinetic energy |
| $G_b$ | Turbulence kinetic energy due to buoyancy |
| $Y_m$ | Compressible turbulence to the overall dissipation rate |
| $\sigma_\varepsilon$ | Turbulent Prandtl numbers for k |
| $\sigma_k$ | Turbulent Prandtl numbers for ε |
| $S_k$ *and* $S\varepsilon$ | User defined source terms. |
| $\mu_t$ | Eddy Viscosity |
| $Y$ | Mass fractions of HCN |
| $Y_{NO}$ | Mass fractions of NO |
| $YNH_3$ | Mass fractions of $NH_3$ |

emissions by 2.5 % for a Toroidal re-entrant combustion chamber (TRCC) geometry when compared to the standard chamber. Several experimental studies are conducted on different piston bowl geometries: hemispherical combustion chamber (HCC) [14–17], shallow depth combustion chamber (SCC) [16], TRCC [18–22], wave-stepped geometry [23], Trapezoidal combustion chamber [24] and many more. For instance, Mamilla et al. [25] observed an increase in BTE by 10.2 % and a decrease in CO, HC, and smoke emissions by 13.3 %, 11.7 %, and 10.1 %, respectively, for the TRCC chamber compared to HCC. In addition, Kumar [26] observed a decrease in BSFC by 8.79 %, an increase in BTE by 2.92 %, and a reduction in HC and CO by 3.19 % and 12.5 %, respectively for the toroidal combustion chamber compared to the baseline chamber. These experimental results revealed that chamber modifications have improved the engine performance and reduced emissions such as CO and HC. However, the nature of combustion inside the chamber is still unpredictable [27]. Though optical studies provide a better understanding of fuel injection and distribution, the analysis of the combustion rate is still challenging to understand. It is hard to investigate and control the rapid combustion rates inside the chamber, but thanks to the computational tools that are helping to observe the combustion behaviour [28].

Significant progress in computational fluid dynamics (CFD) propels research on internal aspects of combustion, complementing experimental-driven studies on combustion rates and emission formation. For instance, Dasrath et al. [29] observed in-cylinder temperature profiles of crevice and bowl chambers using CFD and revealed that bowl chambers had better thermal homogeneity than FCC. In addition, Millo et al. [10] observed jet-to-jet interactions and air–fuel mixture formation in the bowl chambers, which revealed faster flame recirculation near the bowl center region. Furthermore, Nguyen and Dunin [30] reported variations in the spray tip velocities and penetration with the variation of the diameter of bowl chambers. However, there is limited research on the formation of emissions with respect to the combustion profiles. For instance, Sapra et al. [31] investigated the effect of the bowl parameters such as bowl height and radius, lip height and lip radius on combustion behavior using CFD simulations. The study concluded with an optimized combustion chamber based on combustion patterns but left a significant gap in understanding the relationship between chamber design and emission formation rates. Similarly, V and J.M [32], Gianetti et al. [7], Taibani et al. [33], Millo et al. [10] and Xu et al. [34] have explored combustion chamber geometries using the CFD approaches. These studies provided valuable insights into flame distribution, combustion behaviour, and patterns across different geometries. However, they lacked critical information on the impact of bowl geometries on emission formation rates. As discussed above, experimental studies reveal substantial differences in performance among various bowl chamber designs. While some chambers performed well, others did not, suggesting that chamber geometry influences combustion patterns, making them more or less prone to higher emission rates. Although numerical studies have demonstrated significant variations in combustion patterns, there remains a considerable gap in exploring piston bowl designs specifically in terms of their effect on emission formation behavior.

To address the identified gap in understanding the influence of combustion chamber geometries on emission formation, this study aims to develop a turbulent combustion model with chamber modifications to analyze a diesel engine's in-cylinder combustion and emission parameters. A validated diesel engine setup is proposed to perform the complex computational calculations required for non-premixed combustion. The surrogate diesel chemistry (n-heptane) is applied to the modified combustion chambers under validated boundary conditions. Finally, the in-cylinder combustion and emission results from the chamber models are analyzed and discussed, with insights supported by existing literature. The combustion stroke of the in-cylinder parameters has been presented in this study to explore or recommend the chamber with better combustion rates and less emissions. In addition, the air–fuel mixing conditions, fuel distribution, and atomization rates of the

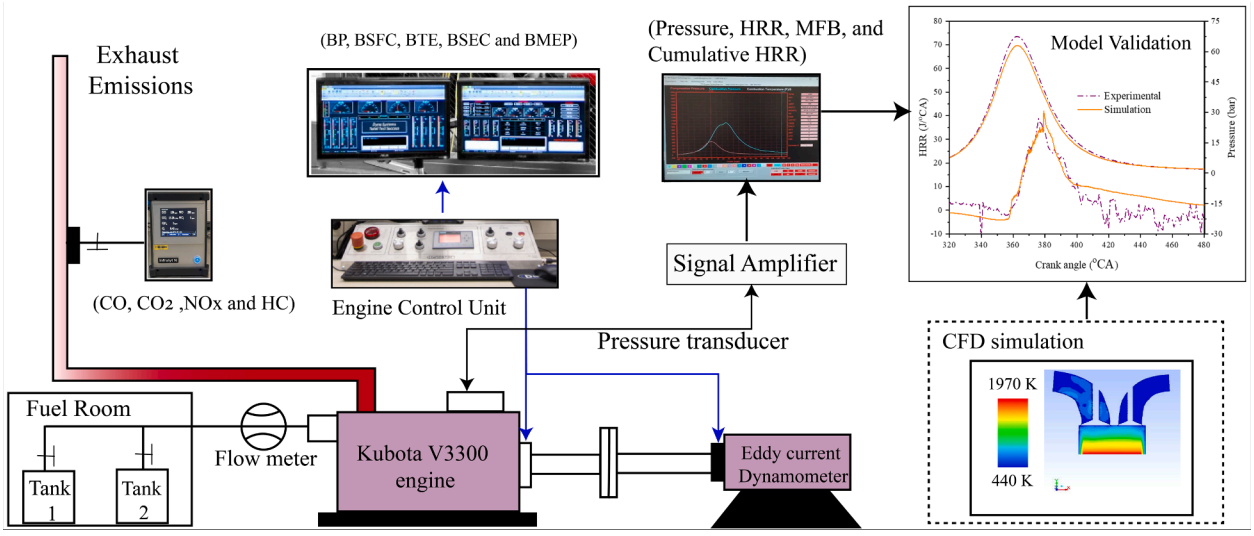


**Fig. 1.** Kubota V3300 Engine test rig schematic diagram.

**Table 1**
Engine Specifications.

| Make | Unit | Kubota V3300 |
|---|---|---|
| Cylinder and cycle | – | Vertical, 4 cycle |
| Type | – | Liquid-cooled diesel |
| Displacement volume | $cm^3$ | 3318 |
| Fuel | – | Diesel |
| Bore × Stroke | cm | 9.8 × 11 |
| Compression ratio | – | 22.6:1 |
| Speed | rpm | 1500 |
| Injection pressure | MPa | 13.73 Mpa |
| Injection timing | – | 16° before TDC |
| IVO | °CA | 243 |
| EVO | °CA | 480 |

injected fuel will be helpful in evaluating which chamber is better suited for practical applications.

## 2. Combustion modelling and simulation

### 2.1. Experimental test setup

Fig. 1 presents the engine test setup, which is controlled by a data acquisition system. The tests were conducted using a 4-cylinder, four-stroke Kubota V3300 commercial engine, with its technical specifications detailed in Table 1. An eddy current dynamometer was connected to the engine to vary the test conditions. The dynamometer is connected to the engine's output shaft, assisting in controlling the rotational speed through resistance. The load conditions varied according to the full throttle position. Before each test, the engine was pre-warmed by running it on diesel fuel for 20 min or until the oil temperature reached 80 °C to stabilize engine conditions and emissions. During the tests, engine torque, speed, and mass flow rates were measured. Performance parameters such as brake power (BP), brake thermal efficiency (BTE), brake specific fuel consumption (BSFC), and brake mean effective Pressure (BMEP) were measured and calculated using standard equations. A fuel flow meter to measure the flow rate of the fuel passing from the tank. A standalone piezoelectric pressure transducer (H32218-GPA, Optrand, MI, USA) was installed on the cylinder head to measure the internal chamber pressure. The pressure data was recorded as an average over one hundred consecutive cycles (from 0 °CA to 720 °CA) and was provided relative to the crank angle degree. Emissions were analyzed using a CODA exhaust gas analyzer (Andros 6241A, California, USA), which employs nondispersive infrared technology to accurately and instantaneously measure emissions such as CO, $CO_2$, HC, and $NO_x$. The parameters were kept constant throughout to ensure comparability across tests. The test was repeated three times to reduce the possibility of random errors, with the mean value reported. More details on data acquisition systems and the accuracy of measurement systems can be found in the authors' earlier studies, Doppalapudi et al. [5] and Doppalapudi et al. [35].

### 2.2. Engine combustion chamber modelling

An IC engine setup was developed using the Ansys fluent software tool with two inlet valves and one exhaust valve that resembles the Kubota V3300 engine attributes, as shown in Fig. 2(a). The test engine has a bore of 98 mm and a stroke of 110 mm. The ports and valves were prepared according to the Kubota manual, and the 3D model was developed using the Ansys space claim tool. A clearance of 0.02 mm was given between the valves and ports for the free flow momentum of fluids inside the chamber [36].

Fig. 2 represents the modelling stages of generating a sector chamber to conduct the combustion simulation. Though the Kubota V3300 engine is a precombustion chamber with two inlets and one exhaust, the study has prepared the chamber as a direct ignition combustion chamber by maintaining the chamber volume with a compression ratio of 22.6:1. Fig. 2(b) shows that a fluid body was extracted from the developed chamber, where all the numerical calculations were carried out. Later, the chamber was decomposed to a sector of 60°, as shown in Fig. 2(c). In the next stage, the layer mesh conditions are applied to the sector chamber, and an adaptively refined mesh is generated, as shown in Fig. 2(d).

### 2.3. Governing equations for simulation and boundary conditions

In IC engine combustion, the combustion parameters are fluid-based entities, and the fluid flows are multi-phase, reactive, and rapid. Hence, Navier-Stokes (RANS) equations have been applied in this study to capture the average flow field from the turbulent motions (flow reactions) under specified boundary conditions. For carrying the simulation, a continuity equation is used to perform the mass conservation inside the combustion chamber with the assumption of no mass gain or loss. In addition, fluid flow influenced by pressure, viscosity, and turbulent forces were calculated using the momentum equations. Where in the IC engine simulation, it is assumed to have consistent thermodynamic properties and often neglects minor losses. Finally, energy changes due to heat release, conduction, and turbulence will be calculated using an energy equation. However, these assumptions may not fully capture the complexities of in-cylinder flows, where phenomena like vortex behaviour and rapid flow occurrences. The governing equations, such as conservation of mass, conservation of momentum, and energy, can be found in the studies Azad et al. [38] and Azad et al. [39].

The swirl ratio inputs are calculated through Equation (1) [40].

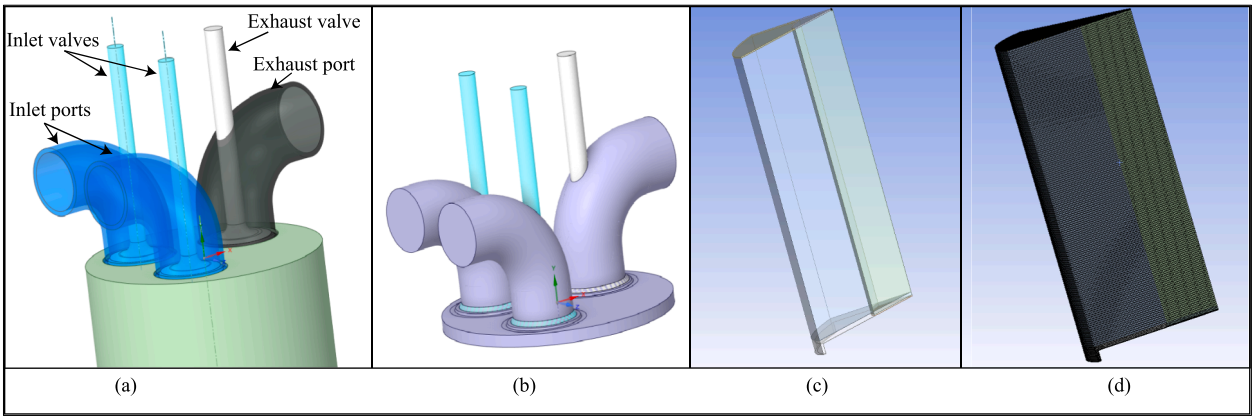


**Fig. 2.** Sector chamber decomposition [37]; (a) Engine chamber model; (b) Fluid volume with valves; (c) Sector decomposed combustion chamber; (d) Mesh-generated combustion chamber.

$$\vec{v} = \vec{r} \times \vec{w} \tag{1}$$

where $\vec{v}$ = *velocity*, $\vec{r}$ = *radial distance*

***Turbulence models***.

Yakhot and Orszag [41] proposed the Re-Normalized Group (RNG) theory aligned with the standard $k-\varepsilon$ model. Here, the $k$ equation is similar to the standard version; however, the $\varepsilon$ equation is from mathematical derivation rather than the empirically derived constants. The $k$-$\varepsilon$ equation is presented as the $k$ equation (equation (2)) and $\varepsilon$ equation (equation (3)) [42 38].

$$\frac{\partial}{\partial t}(\rho k) + \frac{\partial}{\partial x_i}(\rho_1 k u_i) = \frac{\partial}{\partial x_j}\left[\left(\mu + \frac{\mu_t}{\sigma_k}\right)\frac{\partial}{\partial x_j}\right] + G_k + G_b - \rho\varepsilon - Y_M + s_k \tag{2}$$

$\rho$ is density, μ dynamic viscosity,

and

$$\frac{\partial}{\partial t}[\rho_\varepsilon] + \frac{\partial}{\partial x_i}(\rho\varepsilon u_i) = \frac{\partial}{\partial \chi_i}\left[\left(\mu + \frac{\mu_t}{\sigma_\varepsilon}\right)\frac{\partial \varepsilon}{\partial x_j}\right] + c_{1\varepsilon}\frac{\varepsilon}{k}(G_k + C_{3\varepsilon}G_b) - C_{2\varepsilon}\rho\frac{\varepsilon^2}{k} + s_\varepsilon \tag{3}$$

***Spray models***.

At the nozzle inlet passage, liquid fuel volumetric mean flow velocity is calculated using equation (4) [42].

$$U_{Mean} = \frac{\dot{m}}{\rho_{1A}} = \frac{4\dot{m}}{\rho_1 \Pi D^2} \tag{4}$$

where $\dot{m}$ represents the mass flow rate of the fuel, $\rho$ represents density, A and D refer to the nozzle cross-sectional area and diameter.

The discharge coefficient ($C_d$) is used to quantify the losses due to acceleration, formation of the velocity profile at the inlet, expansion after the vena contracta, and wall friction. The $C_d$ equation is shown in equation (5) [42].

$$\mathrm{Cd} = \frac{U_{mean}}{\sqrt{2[p_1 - p_2]/\rho_1}} \tag{5}$$

These governing equations can depict the fluid flow characteristics by directly addressing the computational grid established within the fluid domain of the physical representation. As mentioned earlier, the highly turbulent flow phenomena occurring within the engine cylinder can be effectively simulated utilizing various turbulence models. For instance, the shear-stress transport ($k$-$\omega$) turbulence model introduced by Wilcox in 1978, has shown remarkable performance and is particularly adept at providing precise outcomes in regions close to walls or boundary layers. This model outperforms the k-ε model notably in scenarios involving low Reynolds number flows subjected to adverse pressure gradients [41,43]. However, the $k$-$\omega$ model simulated near the wall flows more appropriately [38]. Hence, the study has chosen k-ε to study cylinder turbulent motions, not just near-to-the-wall motions.

***$NO_x$ transport models***.

Convection, diffusion, generation, and consumption of NO and related species are all considered in the transport equation for the NO species. As a result of being based on the fundamental idea of mass conservation, this strategy is entirely universal. The convection terms in the governing equations given in the Eulerian reference frame include the effect of residence time in $NO_x$ processes (Lagrangian reference frame notion). The NO species transport equation is sufficient for thermal and prompt $NO_x$ mechanisms [42], and the equations are as follows.

$$\frac{\partial}{\partial t}[\rho Y_{NO}] + \nabla\cdot[\rho\vec{v}Y_{NO}] = \nabla\cdot[\rho D\nabla Y_{NO}] + S_{NO} \tag{6}$$

$$\frac{\partial}{\partial t}[\rho Y_{HCN}] + \nabla\cdot[\rho\vec{v}Y_{HCN}] = \nabla\cdot[\rho D\nabla Y_{HCN}] + S_{HCN} \tag{7}$$

where $Y_{NO}$ and $Y_{HCN}$ represents the mass fractions of NO and HCN in the gas phase, and D represents the diffusion coefficient. The source terms $S_{NO}$ and $S_{HCN}$ were later calculated using different $NO_x$ mechanisms. Table 2 summarizes the computational models and methods used in this study for IC engine simulations, focusing on combustion, turbulence, spray breakup, heat transfer, fuel spray, and NOx emissions modeling.

**Table 2**
Summary of model definitions.

| Description | Models used |
|---|---|
| Solver | Non-premixed combustion |
| Turbulence | $k$-$\varepsilon$ model |
| Spray breakup model | Kelvin-Helmholtz / Rayleigh-Taylor (KH-RT) |
| Heat transfer | law-of-the-wall |
| Diesel pilot fuel injection (spray model) | Discrete phase mode (DPM) |
| $NO_x$ emission | Zeldovich |

The cylinder walls and the chamber conditions were kept stationary and maintained at a temperature of 440 K and 560 K. The simulation run is monitored during the combustion stroke, which means the intake valve closing (IVC) to the exhaust valve opening period. The air intake composition and the diesel surrogate CHEMKIN data were added to the setup. Dynamic mesh settings were adjusted using layering and smoothing with 6 degrees of freedom for the chamber walls and piston head surfaces. A mesh sensitivity study must be performed using CFD analysis to determine the numerical accuracy of the calculated results. The discretization error is the error that may be quantified through mesh refinement [44]. The boundary conditions and convergence criteria for

**Table 3**
Boundary conditions and convergence criterion.

| Boundary conditions | values | Residuals | Absolute criteria |
|---|---|---|---|
| Combustion simulation | IVC- EVO | Continuity | 0.001 |
| Sector angle | 60° | x-velocity | 0.001 |
| Cylinder wall motions | Stationary | y-velocity | 0.001 |
| Temperature at chamber top and bottom | 440 K | z-velocity | 0.001 |
| Piston wall temperature | 560 K | Energy | 1e-06 |
| Wall shear condition | No slip | k | 0.001 |
| Injection streams | 50 | epsilon | 0.001 |
| Injection type | Cone | Pollutant NO | 1e-6 |
| Injection particle type | Droplet | Pollutant_$NO_2$ | 1e-6 |
| Spray angle | 70° | | |
| Dynamic mesh | Smoothing and layering | | |

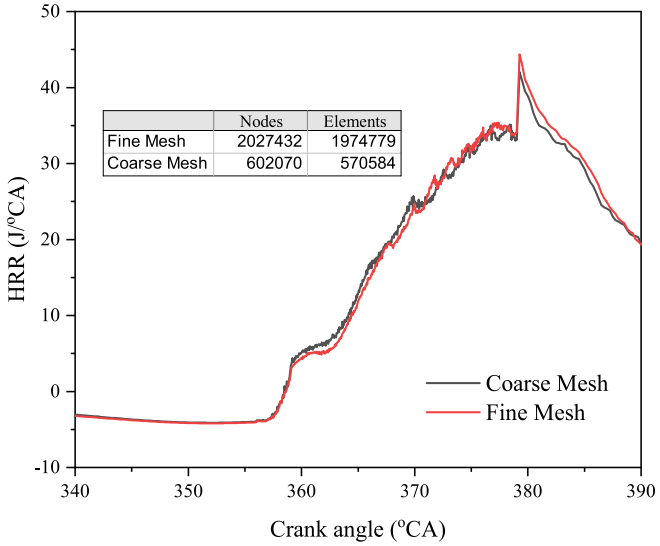


**Fig. 3.** Grid validation of the test setup using HRR.

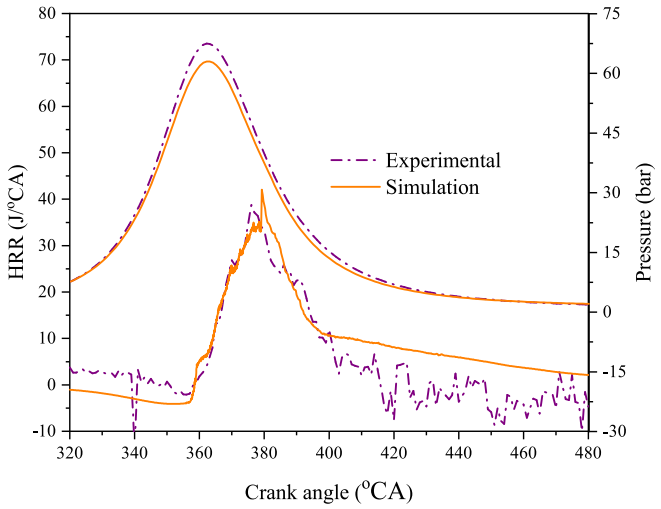


**Fig. 4.** Experimental and simulation HRR and pressure results validation at 1500 rpm.

the model setup are presented in Table 3.

### 2.4. Grid sensitivity test and model validation approach

Fig. 3 demonstrates the marginal influence of mesh types on the outcomes of the combustion simulation. Before validating the setup, a mesh independence test was conducted to assess the impact of mesh parameters on the simulation results. The test was conducted for the FCC chamber to examine the mesh dependency effect on the simulation. First, fine mesh is developed with a sharper resolution using five inflation layers and a reference mesh size of 0.611 mm. The fine mesh has created 20,27,432 nodes and 19,74,779 elements. Similarly, three inflation layers and a reference mesh size of 0.917 mm were used to construct the coarser mesh. In which the coarse mesh created 6,02,070 nodes and 5,70,584 elements. Fig. 3 shows the apparent heat release rates (HRR) of fine and coarse mesh outcomes of HRR for the FCC chamber. The graph indicates that the mesh type has a minimal impact on the engine model simulation. After validating the mesh, modifications were made solely to the injection patterns to further validate the simulation's HRR against experimental data.

Before simulating the model and preparing the modifications to the chamber geometry, it is imperative to validate the correctness and accuracy of the setup. The compression ratio and other key geometrical parameters were set to the manufacturer's specifications to ensure that the model design and setup match the experimental engine. The engine model with two inlet ports and one exhaust port has been developed as per the engine specifications. The dimensions of the valves, the design and angles of the ports, and the locations of the valves have all been designed based on the manual's guidelines. Firstly, the compression ratio of 22.6:1 has been validated by comparing the model's output with experimental data to ensure accuracy. In addition, the computational engine model is benchmarked with experimental data considering HRR and in-cylinder pressure for both cases, and the comparisons are plotted in Fig. 4. The simulation results of both apparent HRR and Pressure computed by fluent code are in satisfactory agreement with the experimental data. The error percentage between the total HRR values of both the simulated and experimental results was approximately 3.8 %, which is below the acceptable tolerance limit of 5 %. The test results show that the experimental and simulated results are validated satisfactorily during the combustion stage. While there were minor disparities in the peak

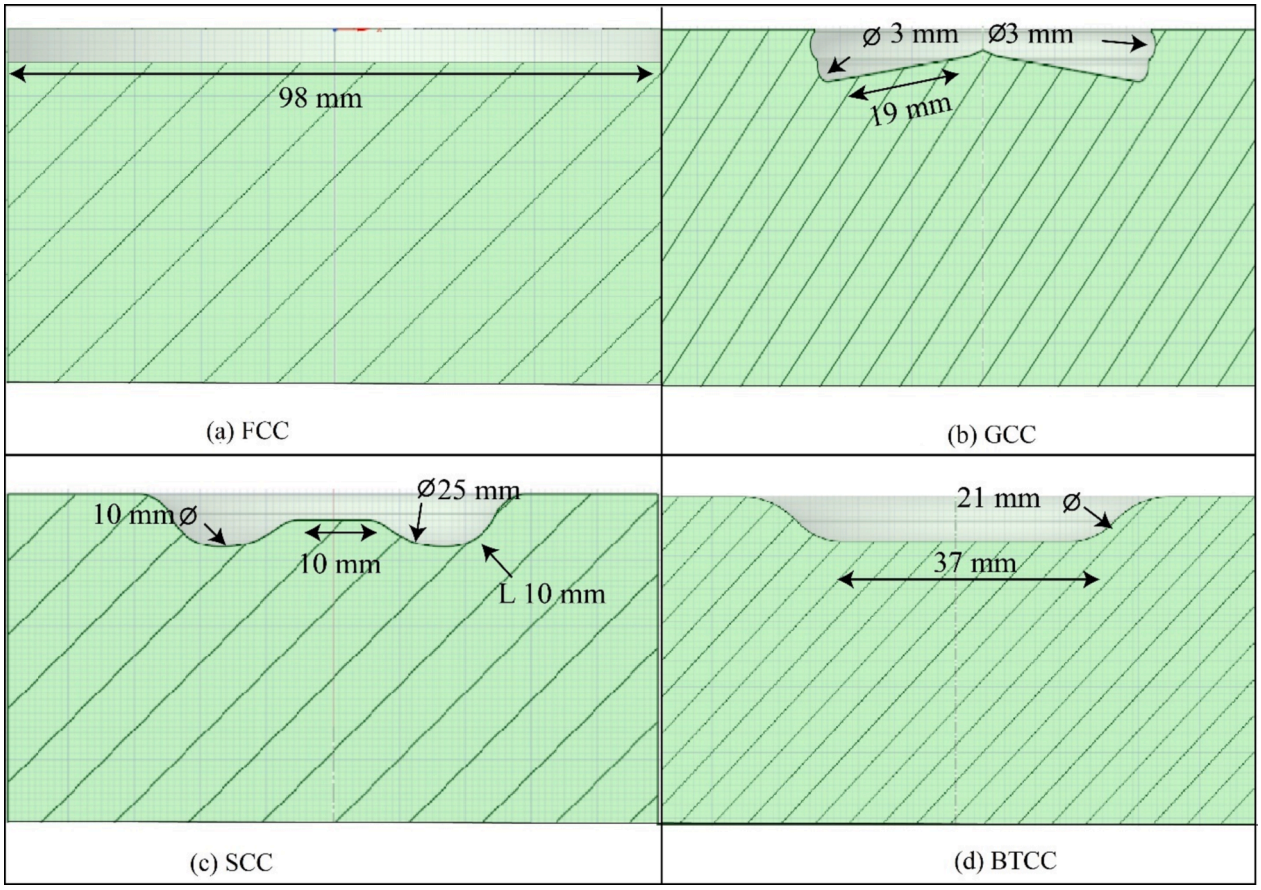


**Fig. 5.** Combustion chamber geometries; (a) FCC; (b) GCC; (c) BTCC; (d) SCC.

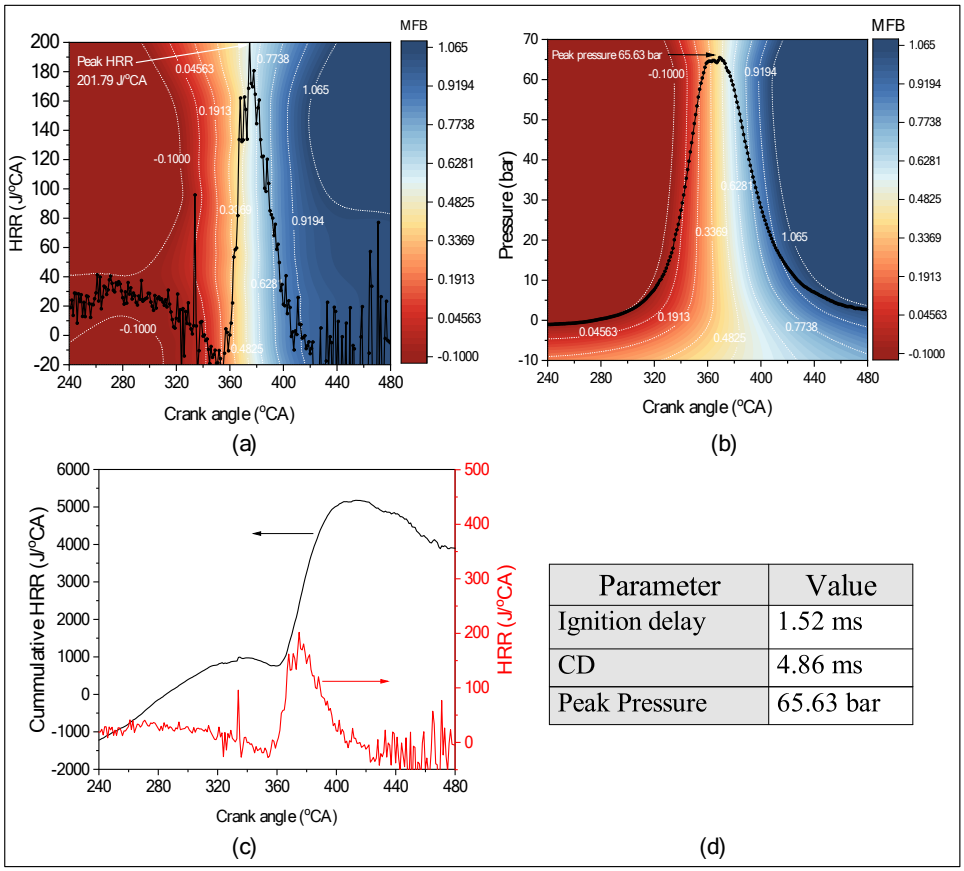


**Fig. 6.** Combustion parameters at 1500 rpm;(a) crank angle vs HRR and MFB; (b) crank angle vs pressure and MFB; (c) crank angle vs CHRR and HRR.

areas of HRR and pressure stages, the combustion pattern behaviors remained consistent throughout the combustion stroke. Also, during the expansion stage, discrepancies in HRR variation were observed between the simulation and experimental data. This difference can be attributed to the simulation's steady decline in HRR, whereas the experimental results exhibited variable decreases in HRR due to complexities in real-world conditions frictional, and combustion factors [45].

### 2.5. Chamber geometry modifications

As mentioned earlier, the clearance volume of the flat chamber was adjusted while keeping the test engine's compression ratio and displacement volume unchanged. Fig. 5 presents the design of bowl shapes, grooved combustion chamber (GCC) inspired by the re-entrant combustion chamber [15], bathtub combustion chamber (BTCC) inspired from Benajes et al. [46] and shallow depth combustion chamber (SCC) inspired from Ranganatha Swamy et al. [47]. To maintain uniformity, the above-mentioned simulation setup was applied for these modified chambers while keeping the same operational settings, injection parameters, material inputs and boundary conditions.

## 3. Results and Discussions

### 3.1. Experimental test results analysis

The engine test results were considered at 1500 rpm to investigate the formation of emissions at medium load conditions. The inefficiency or hotspots of the combustion formation can be easily understood at medium speed ranges than low and high speeds. Simulating at lower speeds can limit the influence of turbulence, especially with chamber modifications. On the other hand, at high speeds, friction losses and heat transfer rates are the dominating factors in experimental operation. From the authors' earlier studies, Doppalapudi et al. [5], the BTE and $NO_x$ emissions were increased from 1200 rpm to 1800 rpm and then started decreasing from 1800 rpm to 2400 rpm. Hence, simulating at 1500 rpm allows to analyze combustion rates and emissions in a critical range where emissions are rising stage, making it an essential point for capturing relevant combustion and emission characteristics. For instance, Guo and Liko [48] observed stable combustion at medium to high load conditions as long as the injection was appropriately adjusted.

Meanwhile, the combustion duration, flame propagation speed, and combustion temperature were much higher in high-load conditions [48]. The fuel mixing rate, incomplete combustion, emission formation, and injection fine-tuning can be easily investigated when the engine is operated at mid-range speed conditions. The study has opted for 1500 rpm to investigate the combustion efficiency and impact of CO, $CO_2$, HC, and $NO_x$ formations. At 1500 rpm, with the performance parameters, where the engine has shown brake power (BP) of 35 kW, a brake specific fuel consumption (BSFC) of 0.254 kg/kWh, a brake mean effective pressure (BMEP) of 8.61 bar, a brake thermal efficiency (BTE) of 33.16 %, and a fuel conversion efficiency (FCE) of 33.2 %. The emission parameters were recorded as carbon monoxide (CO) emission of 1148 ppm, carbon dioxide ($CO_2$) formed at 11.07 % by volume, hydrocarbons (HC) emission of 28 ppm, oxygen ($O_2$) with 39.01 % by volume of the total exhaust gases, and nitrogen oxides ($NO_x$) emission of 234 ppm.

Fig. 6(a), (b), (c) and (d) show the experimental results of combustion parameters of in-cylinder Pressure, HRR, MFB, and cumulative HRR (CHRR) at 1500 rpm. The combustion parameters were presented from the inlet valve closing time of 243 °CA to the exhaust valve opening time of 480 °CA. In the initial phase of combustion, negative heat release is observed because the fuel undergoes vaporization during the ignition delay period. Once combustion has started, the rate of heat release is increased [49]. At 1500 rpm, peak HRR 197 J/°CA was noticed at 375°CA, whereas peak pressure 65.63 bar was noticed at 370°CA.

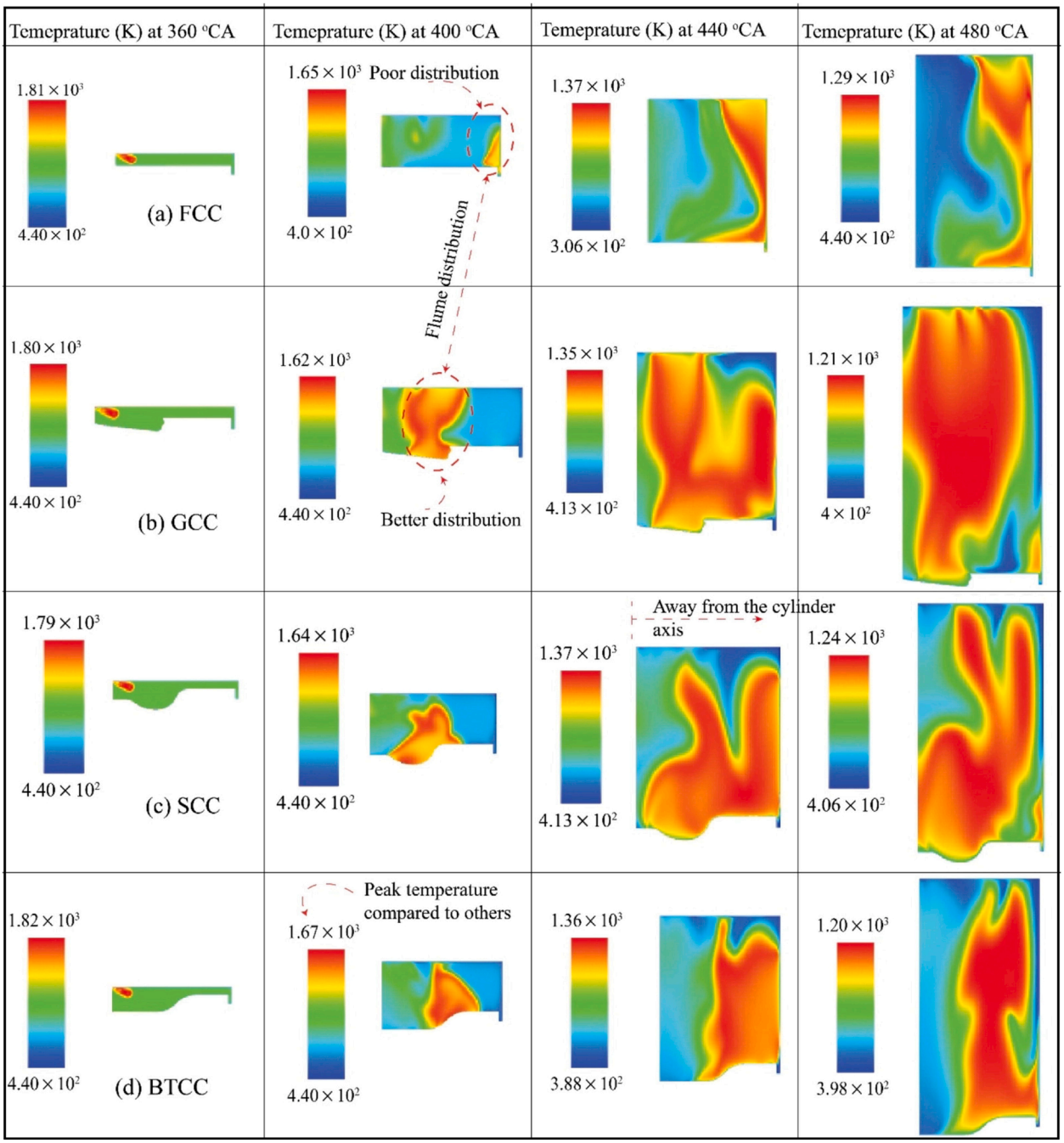


**Fig. 7.** Temperature contours of a cut plane for different piston bowl chambers at respective crank angles.

However, with the increase in speeds, the HRR value also increases. From the authors' earlier studies, the peak HRR for the diesel is noted as 199.97 J/°CA and 249.576 J/°CA, respectively, for the speeds of 1600 rpm and 2000 rpm [50]. Similarly, peak pressure was also noted as 67.23 bar and 69.23 bar, respectively, at 1600 rpm and 2000 rpm. However, a decline in peak HRR and peak pressures was noticed due to shorter combustion duration, limiting the time for the complete combustion [5]. As can be seen from the comparisons Fig. 6(a) and (b), the majority of the mass fraction bunt happened before the peak pressure was obtained. The smooth slope of the MFB curve, together with the HRR peak, aligns with a combustion duration of 4.86 ms. This indicates that the combustion is completed efficiently over an appropriate time window, maximizing energy release without extending too far into the expansion stroke. From this investigation, the study wants to examine the combustion parameters to assess how effectively the simulation investigations can predict the rate of fuel burning, apparent HRR, and pressure, which are crucial for exhaust emissions.

### 3.2. Effect of chamber modifications on combustion parameters

#### 3.2.1. Effect of chamber modifications on in-cylinder temperature

Fig. 7 shows the temperature contours for the FCC, GCC, SCC, and BTCC chambers at 360 °CA, 400 °CA, 440 °CA and 480 °CA. FCC showed poorer combustion formation but still depicted higher temperatures of 1370 K and 1290 K at 440 °CA and 480 °CA, respectively. Because of the flat surface of FCC, the plumes were passed towards the cylinder walls and caused improper fuel distribution (which can lead to improper combustion) near the wall region [51]. As can be seen, the localized high-temperature region was clearly impacted by the inefficient air–fuel mixing. Next to FCC, SCC has shown peak temperatures, followed by

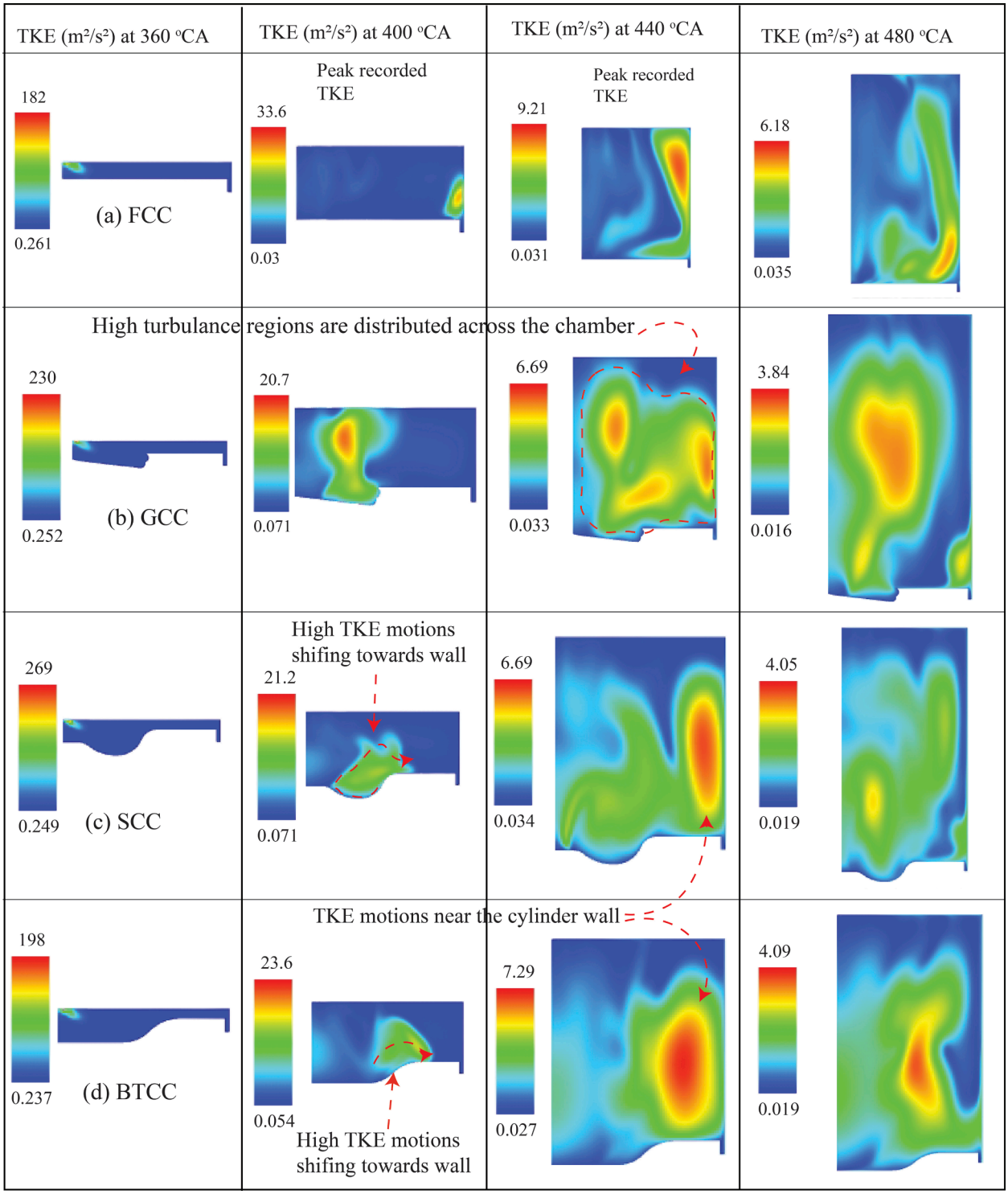


**Fig. 8.** TKE contours of a cut plane for different piston bowl chambers at respective crank angles.

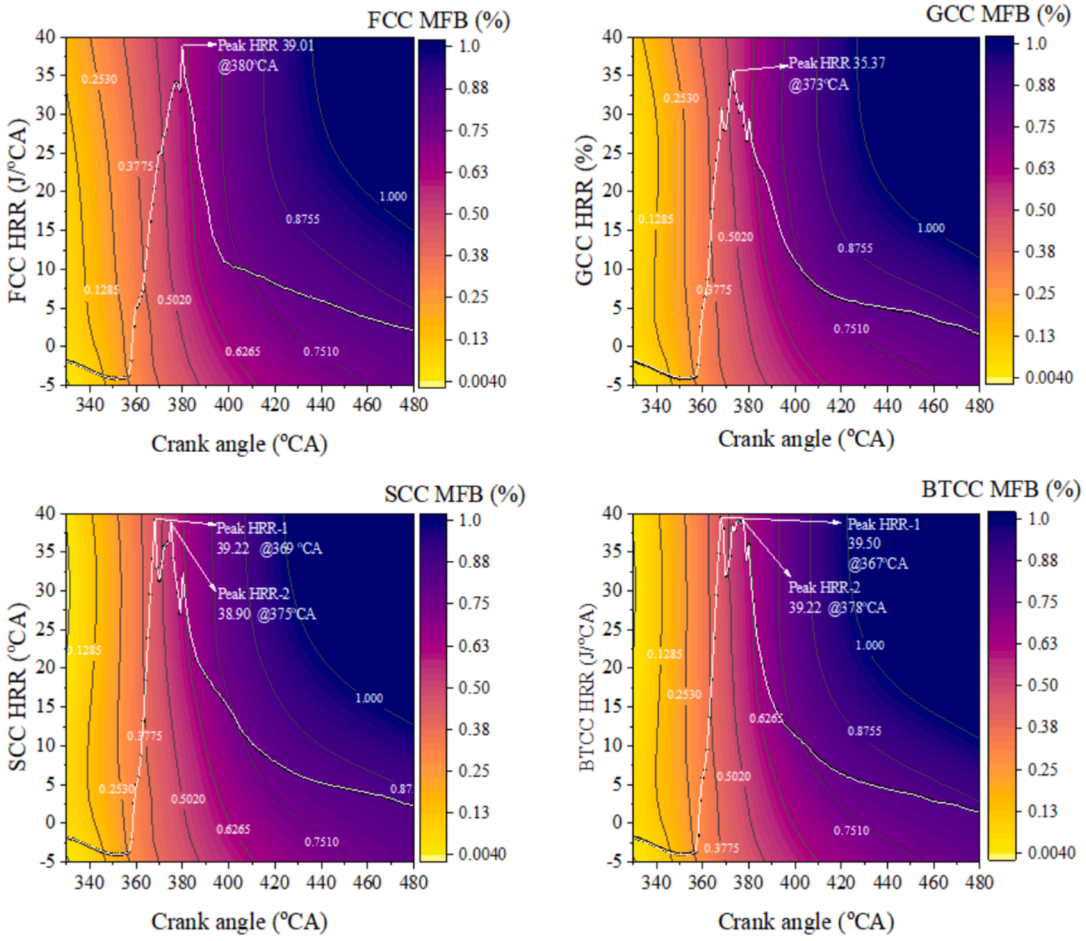


**Fig. 9.** Heat release rate plots for different chambers with respect to the crank angles.

BTCC and GCC. There is no apparent uniform temperature distribution for all the chambers; however, the GCC chamber showed better temperature distribution than others (red contour zones from the cylinder axis to the wall). Grooves of GCC enhanced some level of turbulence. However, the temperature remains localized, indicating that flame propagation is still limited, and thus the temperature distribution becomes even at the later crank angle. In addition, with the SCC, a swirling behaviour can be seen on the temperature contours. The swirl motions inside the chamber influence the uniform distribution of the temperatures and improve the combustion efficiency. Finally, BTCC has also shown better distribution inside the chamber. Compared to other chambers, the distribution is well confined with the increasing crank angles. However, the cooler spots suggest that the flame is still not distributed well, resulting in improper distribution.

From the results, it is understood that maintaining temperature uniformity is very difficult during the combustion stroke. For instance, FCC has shown peak departure of 1650 K at 400 °CA, compared to other chambers, 1620 K and 1640 K for GCC and SCC chambers. However, the paramount consideration to note is that the high-temperature regions are less extensive in FCC than others. This poor distribution of fluids in the FCC chamber will lead to higher unburnt hydrocarbon emissions. Though combustion-wise, GCC, SCC, and BTCC showed better distribution, there is a greater chance of higher NOx emissions for these chambers than for FCC. Similar behavior also can be observed for the crank angles 440 °CA and 480 °CA. This is due to the improved fuel evaporation rates with the flat-with-center-bowl piston [52]. The temperature distribution for all the chambers appears to depend on the injected fuel flumes [53,54]. The high-temperature region occurrences were observed along the injected fuel path. The bowl chambers have provided better fuel distribution, hence the better temperature distribution compared to the standard FCC chamber. In the case of actual experimental combustion activities such as heat transfer through the cylinder walls, flame-wall interactions, and turbulence, which may not be fully captured in the simulation. In addition, as discussed earlier, the $k-\varepsilon$ turbulence model can not fully capture the local temperatures, especially near walls. Overall, the combustion phenomenon and how geometry influences combustion and chamber optimization can be clearly understood with the simulations.

### 3.2.2. *Effect of chamber modifications on the turbulent kinetic energy*

Fig. 8 illustrates the developments of TKE distribution during the in-cylinder combustion process for different combustion chambers at crank angles 360 °CA, 400 °CA, 440 °CA and 480 °CA, respectively. TKE plays a major role in the air–fuel mixing process [55]. Fig. 7 depicts that higher TKE zones are generated for the modified chambers than for the standard chamber. Regardless of the peak TKE, the modified chamber showed better TKE across the chambers compared to FCC. The interaction between squish and swirl flows in the central region significantly contributes to TKE generation [56]. The relatively high TKE values in the central region and near the injection point bowl geometries promote early flame propagation, leading to rapid charge combustion and faster heat release [57]. Because of the grooved chamber for GCC, the fuel flumes are dispersed at the center of the bowl and squish regions. The collision of the higher-momentum mixture with the cylinder head aids its penetration into the central and squish zones [58]. Meanwhile, for FCC, SCC, and BTCC, a higher TKE was observed in the squish area. This is mainly due to the slipping of the high turbulent motions to squish regions by following the trajectory profiles of the combustion formation

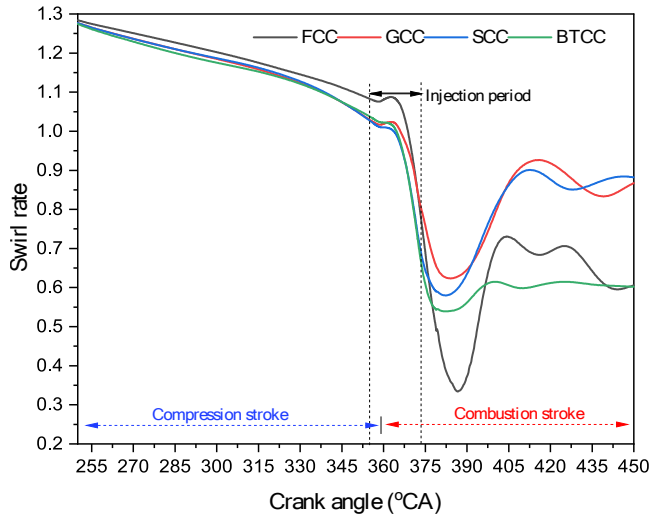


(a)

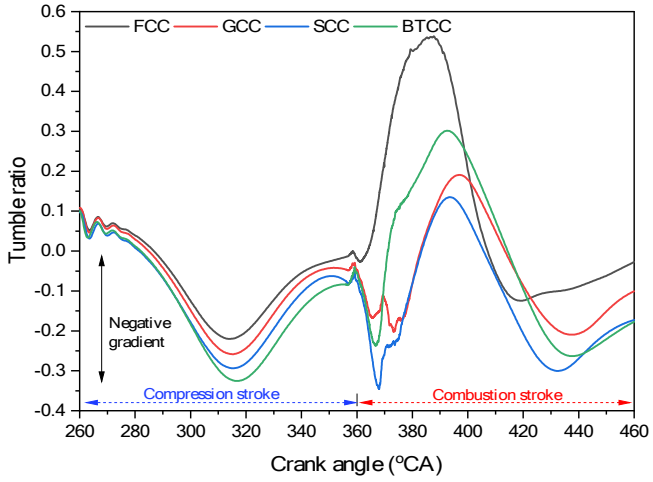


(b)

**Fig. 10.** Effect of chamber modifications on in-cylinder motions with respect to the °CA; (a) Swirl ratio; (b) Tumble ratio.

with respect to the injected fuel combustion formation. At 440 °CA and 480 °CA, FCC revealed TKE of 9.21 $m^2/s^2$ and 6.18 $m^2/s^2$. Whereas for GCC (6.69 $m^2/s^2$ and 3.84 $m^2/s^2$), SCC (6.69 $m^2/s^2$ and 4 $m^2/s^2$) and BTCC (7.29 $m^2/s^2$ and 4.09 $m^2/s^2$) were recorded at the same crank angles. The progressive increase in TKE from 360 °CA to 480 °CA in all cases demonstrates the combustion process, where pressure and temperature build-up, leading to more intense and turbulent conditions [59]. Due to the bowl profile of GCC and SCC, high and distributed TKE zones are recorded in these zones. Because of the chamfered bowl, the TKE zones are shifted towards the squish regions, thereby generating the peak TKE compared to GCC and SCC. GCC has utilized both bowl and squish regions for the turbulent mixing of the particles, allowing homogeneous combustion and higher heat release [60].

### 3.2.3. *Effect of chamber modifications on the HRR and mass fraction burnt*

Fig. 9 demonstrates the HRR at different crank angles for different combustion chambers. It can be seen from the HRR graph that the FCC curve moves towards the expansion stroke, whereas the modified chambers have shown early combustion. Peak HRR is noticed for FCC at 380 °CA, whereas the peak HRR for GCC, SCC and BTCC were noticed early. The slow and improper distribution of combustion rates has caused delayed ignition in the FCC chamber and created lower local temperature zones. This is the main reason the HRR moved towards expansion stroke for the FCC chamber. The modified chambers have shown shorter ignition delay because of the high TKE, which causes rapid air–fuel mixing. Usually, rapid combustion (shorter ID) takes place with premixed conditions with the given fuel. However, chamber modifications contribute to faster evaporation of diesel fuel droplets and cause shorter ID. Due to the shorter bowl height of the GCC chamber, the fuel pockets are formed on the cylinder head and bowl places, which have caused lower heat release rates than the others. GCC has the lower premixed combustion, allowing the peak HRR to reach at 373°CA. However, from the temperature and TKE profiles, GCC has a slightly improved diffusion combustion compared to other modified chambers. In the case of SCC and BTCC, two peak HRR rates were observed. For instance, SCC showed a higher peak HRR of 39.22 J/ °CA at 369 °CA, whereas the second peak was observed at 375 °CA with an HRR value at 38.90 J/ °CA. Premixed combustion has occurred for the SCC and BTCC chambers, allowing for the small ID.

### 3.2.4. *Effect of chamber modifications on the swirl and tumble ratio*

Fig. 10 represents the swirl and tumble motions generated inside the chambers at different crank angles. Swirl and tumble motions play a vital role in creating turbulent motions inside the chamber, influencing the air–fuel mixing process. As shown in Fig. 10(a), high swirl motions are generated during the compression stroke, whereas these motions gradually decrease during the injection period and increase again in the combustion period. During the combustion period, higher swirl rates are observed for the modified chambers than for FCC. Besides, the GCC and SCC showed higher swirl rates compared to the other chambers. Fig. 10 (b) shows the tumble ratio for the different chambers at different crank angles. FCC has shown a higher tumble ratio compared to all the other chambers. Similar results are also observed in the report by Harshavardhan and Mallikarjuna [61]. This is due to the higher TKE of the particle motions inside the cylinder chamber, causing higher tumble motions during combustion stroke [62]. It is predicted from Fig. 8 that the rate followed by the swirl and tumble motions are inversely proportional. A negative gradient is observed during the compression stroke, where the tumble ratio gradually increases during the injection period and then decreases along the combustion stroke.

## 3.3. *Effect of chamber modifications on emission parameters*

### 3.3.1. *Effect of chamber modifications on the fuel mass fraction*

The mass fractions $(\frac{kg_{fuel}}{kg_{mix}})$ of surrogate diesel fuel during the combustion stroke are presented in Fig. 11. According to the results, relatively lower mass fractions were achieved for the modified chamber than the standard FCC chamber. With the modified chambers, the improved air–fuel mixing rates have enhanced the combustion process and reduced the mass fractions inside the chamber [63]. Whereas higher mass fractions with the FCC are due to the wall-wetting nature of the injected fuel [64]. The high injection fuel pockets are situated on the wall, causing improper distribution and affecting the combustion rates [65]. The results clearly illustrate that complete combustion has not happened for all the chambers, but the modified chambers showed fewer mass fractions than the standard chamber. In the case of the FCC and GCC chamber, the fuels get stuck on the top of the chamber head because of the no /lower bowl depth. This spray impingement is due to the obstruction of fuel spray momentum for FCC and GCC chambers, leading to earlier contact with the cylinder head compared to the shallower type chamber [66]. As a result, combustion partially quenches, resulting in a lower peak heat release rate during the premix phase. The groove profile

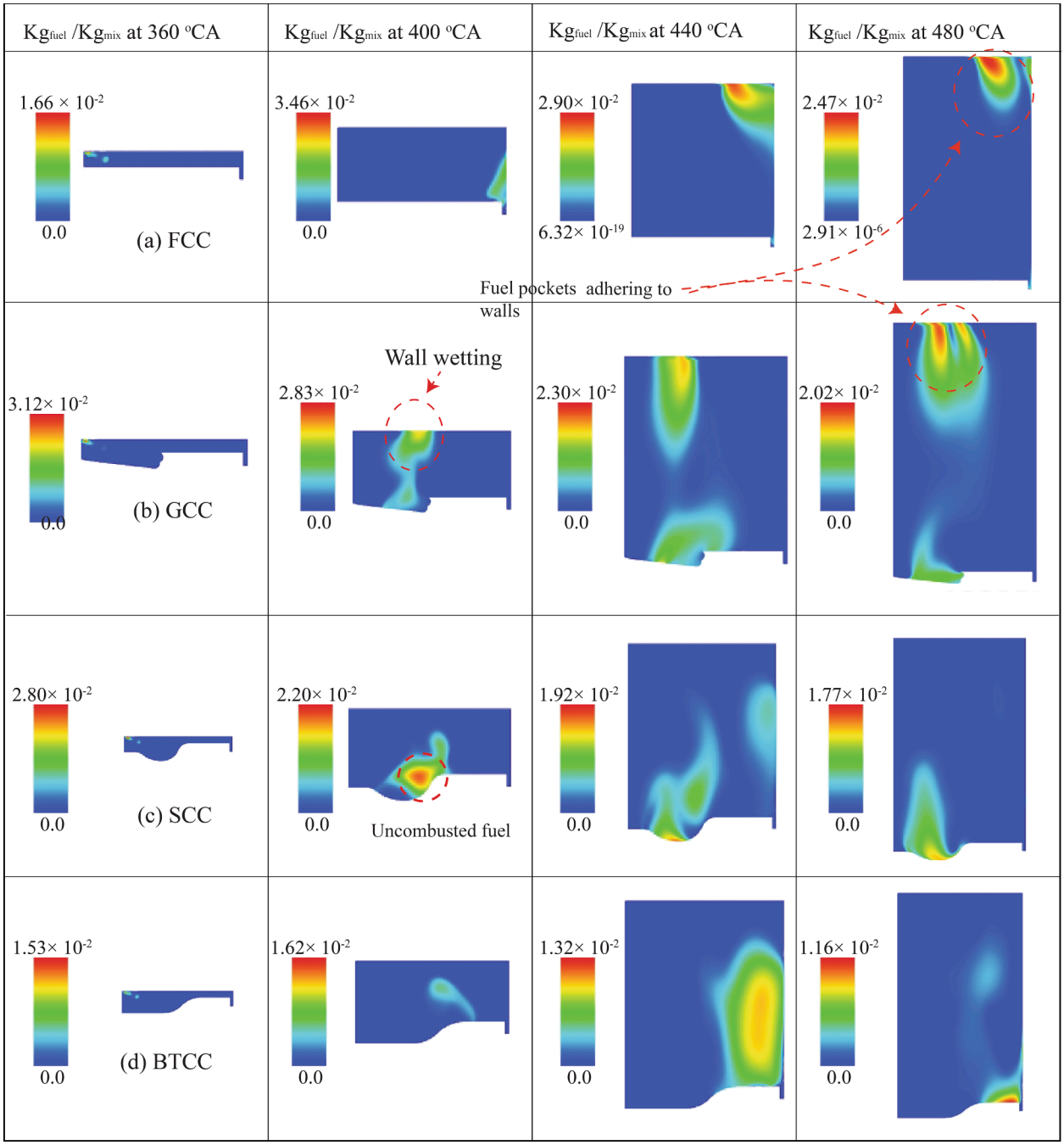


**Fig. 11.** Mass fraction contours of a cut plane for different piston bowl chambers at respective crank angles.

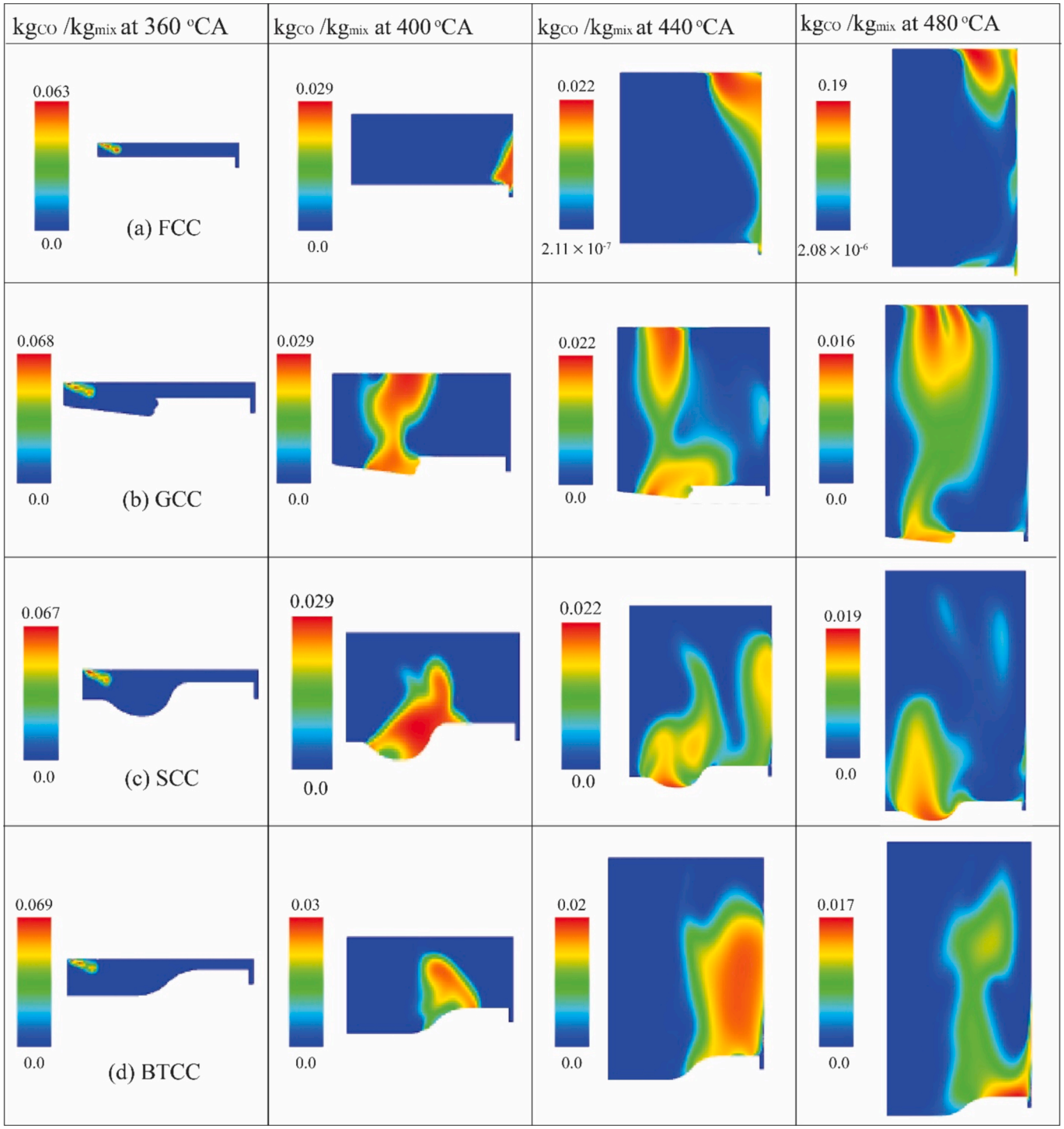


**Fig. 12.** CO emissions contours of a cut plane for different piston bowl chambers at respective crank angles.

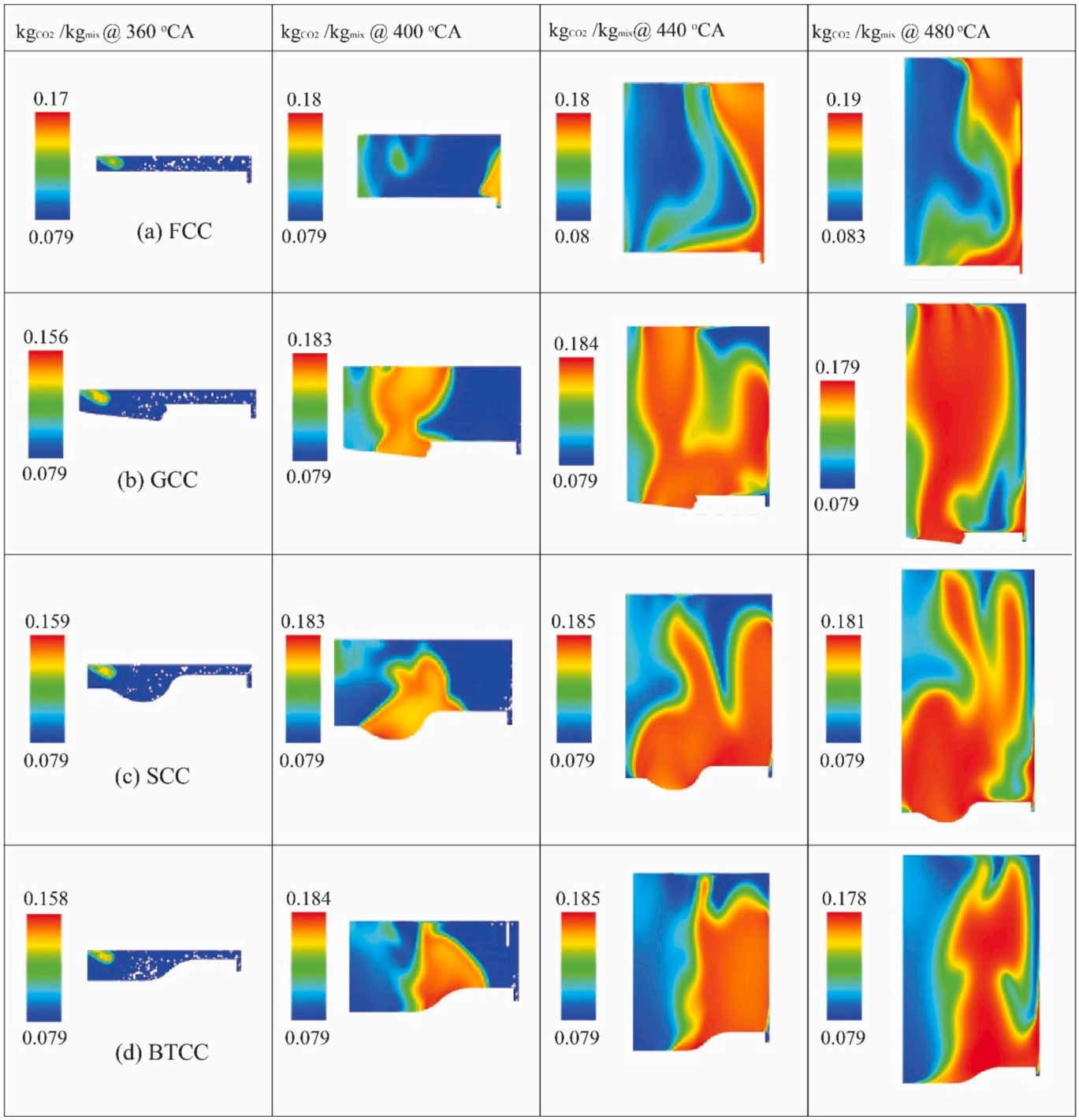


**Fig. 13.** $CO_2$ emissions contours of a cut plane for different piston bowl chambers at respective crank angles.

of GCC directs a larger portion of the mixture to the squish regions, reducing the localized mixture near the bowl areas and enhancing effective premixed combustion [58]. Due to the longer bowl depth of the SCC chamber, the fuel combustion was situated at the centre of the chamber. However, a small amount of fuel was stuck inside the bowl chamber, which led to incomplete combustion. BTCC has shown better combustion, as the fuel slipped from the bowl to the squish regions and has caused less unburnt mass fractions in the chamber. At 480 °CA, BTCC ($1.66 \times 10^{-2}$ $\frac{kg_{fuel}}{kg_{mix}}$) has shown small mass fractions compared to SCC ($1.77 \times 10^{-2}$ $\frac{kg_{fuel}}{kg_{mix}}$), GCC ($2.02 \times 10^{-2}$ $\frac{kg_{fuel}}{kg_{mix}}$) and FCC ($1.47 \times 10^{-2}$ $\frac{kg_{fuel}}{kg_{mix}}$) chambers.

### 3.3.2. *Effect of chamber modifications on CO emissions*

The CO emission ($\frac{kg_{CO}}{kg_{mix}}$) for different combustion chambers at various crank angles are presented in Fig. 12. There is a strong correlation between the patterns of fuel mass fraction (Fig. 11) and CO emissions (Fig. 12). During the compression stroke (360 °CA), peak CO emissions for the GCC, SCC, and BTCC are increased compared to FCC by 6.96 %, 6.01 % and 8.66 %, respectively. Moreover, the peak CO emissions at 400 °CA for FCC, GCC, SCC, and BTCC decreased by 54.11 %, 57.4 %, 56.72 %, and 57.56 %, respectively, compared to peak CO emissions at 360 °CA. Though the peak emissions are higher at 360 °CA, the higher concentrations (expanded CO-rich zones) are noticed at 400 °CA and

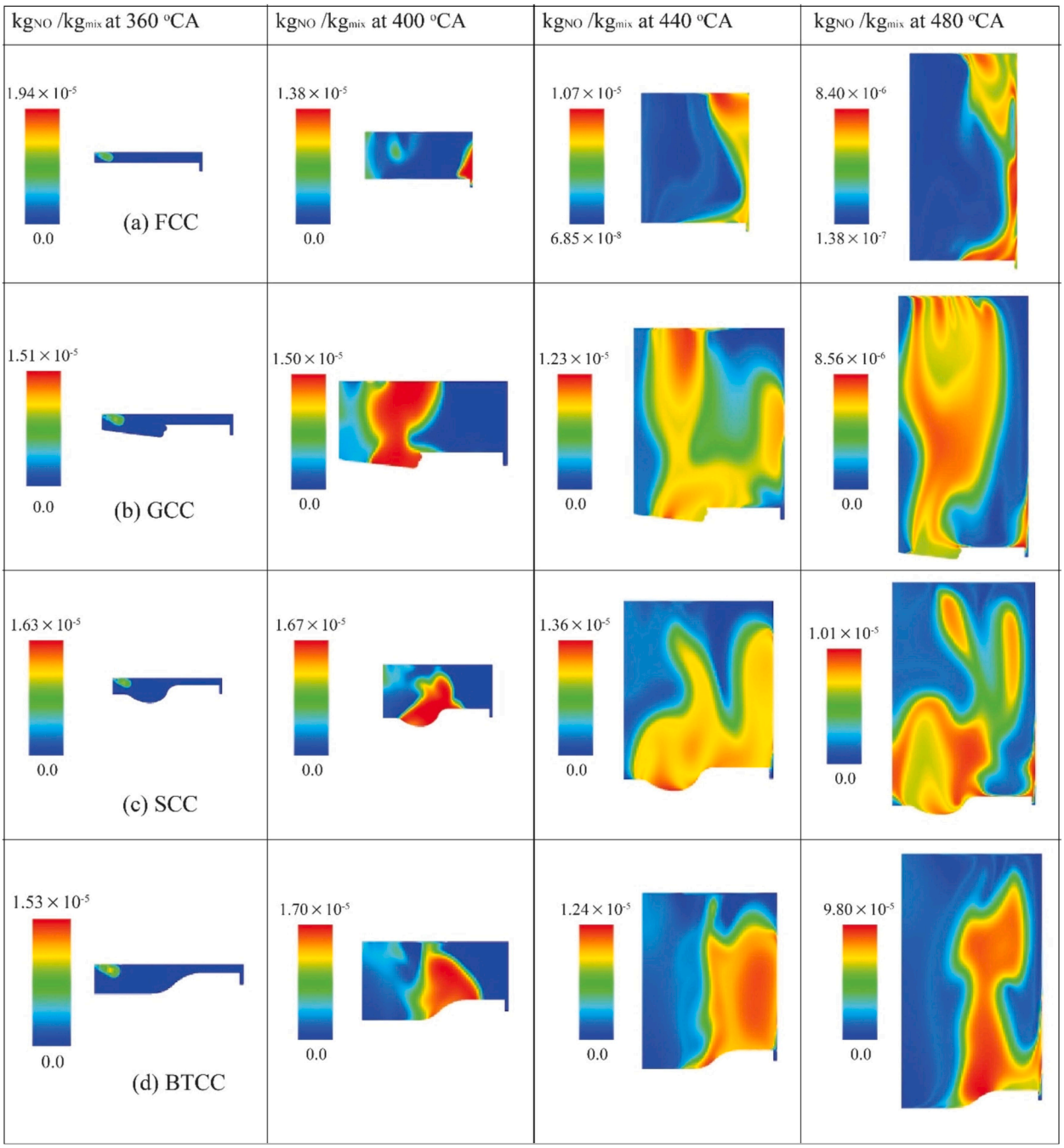


**Fig. 14.** NO contours of a cut plane for different piston bowl chambers at respective crank angles.

440 °CA. Higher CO emissions are detected where high fuel mass fractions are formed. The formation of CO pollutant emissions increases due to insufficient oxygen in the in-cylinder over-rich regions. Additionally, a significant amount of CO pollutants can also be produced in highly lean mixtures and low-temperature regions (typically below 1500 K in-cylinder temperature) [67]. Calam et al. [68] observed that as engine load increases, the additional fuel injected into the cylinder lowers the air/fuel ratio and raises CO emissions. Similar results are also noticed in studies by Prabhu et al. [69] and Gulcan and Ciniviz [13]. Fewer CO concentrations are observed for FCC chambers at 360 °CA and 400 °CA. This is because mixings-combustion might not occur due to improper air–fuel mixing. Incomplete combustion with insufficient oxygen causes high CO emissions during combustion for rich fuel mixtures. DSCC showed the highest CO emissions compared to all the other chambers, followed by the BTCC, FCC, and SCC chambers.

### 3.3.3. *Effect of chamber modifications on the $CO_2$ emissions*

The mass fractions of $CO_2$ ($\frac{kg_{CO2}}{kg_{mix}}$) emitting from the different modified chambers at different crank angles are presented in Fig. 13. The spatial distribution contours of the $CO_2$ clearly match the temperature profiles. This is because of the oxidation of CO emissions to $CO_2$ at high temperatures. $CO_2$ emissions are formed around the high-temperature zones. In the experimental tests conducted by Channappagoudra et al. [70], lower CO emissions are observed for the toroidal piston bowl shape compared to the standard chamber. The study reported that improved air motions inside the bowl chamber have helped the oxidation of CO to $CO_2$ emissions. Peak $CO_2$ emissions at 360 °CA increased by 7.6 %, 14.75 %, 13.11 % and 14.13 %, respectively, compared to emissions at

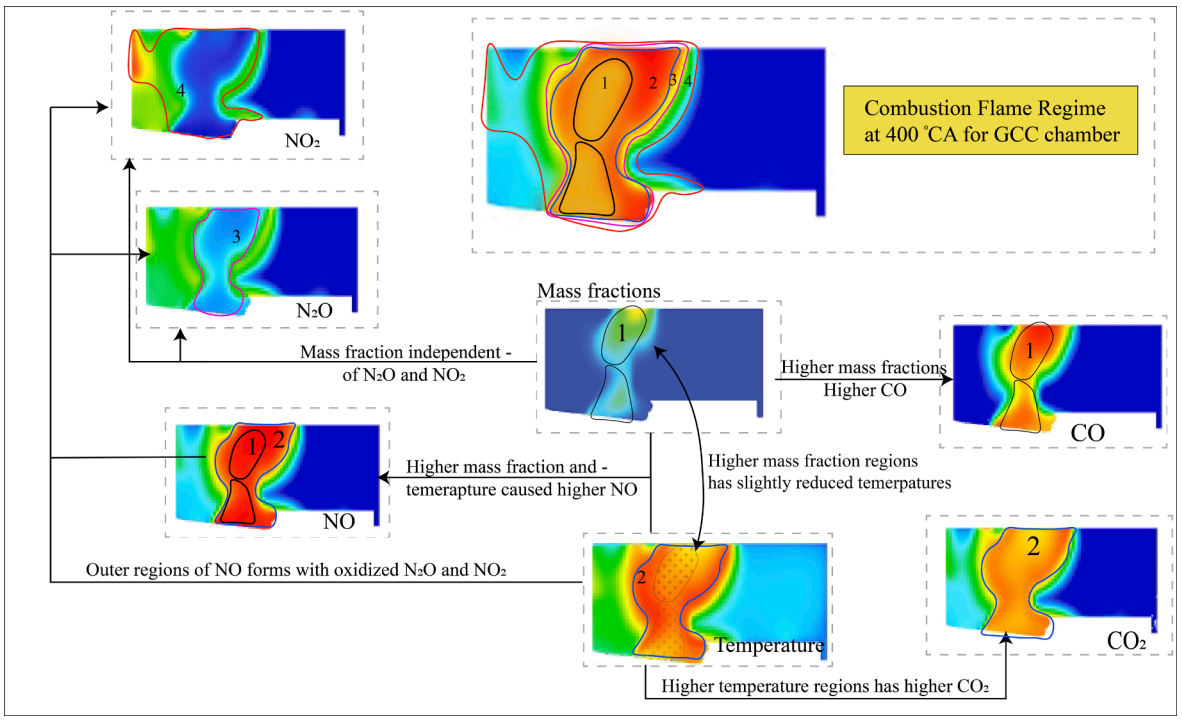


**Fig. 15.** Comparison of combustion parameters with the emission parameters for GCC chamber at 400 °CA.

400 °CA. Rich $CO_2$ zones are more common in GCC, BTCC, and SCC than in FCC chambers. This is because of the high-temperature profiles caused by the high turbulent motions inside the modified chambers. Similar results are also found in studies by Pham et al. [71] and Al-Abboodi [72]. For the GCC chamber $CO_2$ emissions increase significantly in the grooved regions and become more widespread across the combustion stroke. Meanwhile, for SCC, due to the bow shape, the $CO_2$ ratio increases, particularly in the central region, and becomes more uniform and higher. The piston bowl geometries affect the combustion dynamics and elevate the $CO_2$ emissions across the combustion stroke.

### 3.3.4. *Effect of chamber modifications on the $NO_x$ emissions*

Fig. 14 shows the NO ($\frac{kg_{NO}}{kg_{mix}}$) emission contours for FCC, GCC, SCC and BTCC chambers at different crank angles. NO emissions are higher for modified chambers compared to the standard FCC chamber. From the results, it is depicted that NO emissions (Fig. 14) are high in high-temperature zones (Fig. 7), high fuel–air mixture zones (Fig. 10) and high TKE zones (Fig. 7). Duan et al. [73] observed NO fraction of over and above 97 % and $NO_2$ at about 2 % of total $NO_x$ from a CI engine simulation model. According to Zeldovich, thermal NO emissions are formed when nitrogen and oxygen react at higher temperatures, as shown in reactions (8) and (9).

$$N + O_2 = NO + O \tag{8}$$

$$N_2 + O = NO + N \tag{9}$$

Later, the reaction was modified by considering the free OH radicles and the extended Zeldovich reaction is represented in the reaction (10).

$$N + OH = NO + H \tag{10}$$

As NO emissions are highly dependent on temperature conditions, the NO emission contours and temperature contours are quite similar. SCC showed higher NO emissions compared to GCC and BTCC. At 400 °CA, peak NO emissions for GCC, SCC, and BTCC increased by 8.7 %, 21 %, and 23.9 %, respectively, compared to the FCC chamber. NO emissions are formed in high-temperature areas and excessive air regions. GCC showed higher $NO_x$ emission ratios in the combustion cycle, especially around the central region, due to enhanced mixing and air–fuel interactions facilitated by the grooved design. This design promotes localized high-temperature regions conducive to $NO_x$ formation [74]. SCC exhibits low initial $NO_x$ values, but as combustion progresses, the central region shows increased activity, reflecting moderate combustion and mixing efficiency, leading to higher $NO_x$ emissions. BTCC, with its bowl design, shows significant $NO_x$ activity around the bowl region, indicating strong turbulence and efficient combustion due to the effective swirl and squish interactions promoted by the bowl shape. These interactions result in localized high temperatures, which increase $NO_x$ formation.

### 3.3.5. *Effect of combustion parameters on $NO_x$ emissions*

The variations in the combustion chamber mainly influence temperature profiles and mass fraction distributions. This leads to the formation and concentration of different emissions. For a clear understanding of the combustion parameters and emissions characteristics, the GCC chamber at 400 °CA and the SCC chamber at 440 °CA are considered as references and presented in Figs. 15 and 16. Zones 1, 2, 3, and 4 are designated based on the combustion and combustion formations. The combustion zones are defined by different temperatures and reaction characteristics. High-temperature zones (e.g., Zone 1) typically result in higher NO formation due to the thermal NO mechanism. The temperature profiles directly influence the formation of NO, $NO_2$, and $N_2O$ [55]. Higher temperatures promote the formation of these oxides of nitrogen. The formation of $NO_2$ and $N_2O$ in the outer regions indicates secondary reactions where NO reacts with $O_2$ or other species to form these compounds. The formation of $NO_2$ from $N_2O$ suggests that

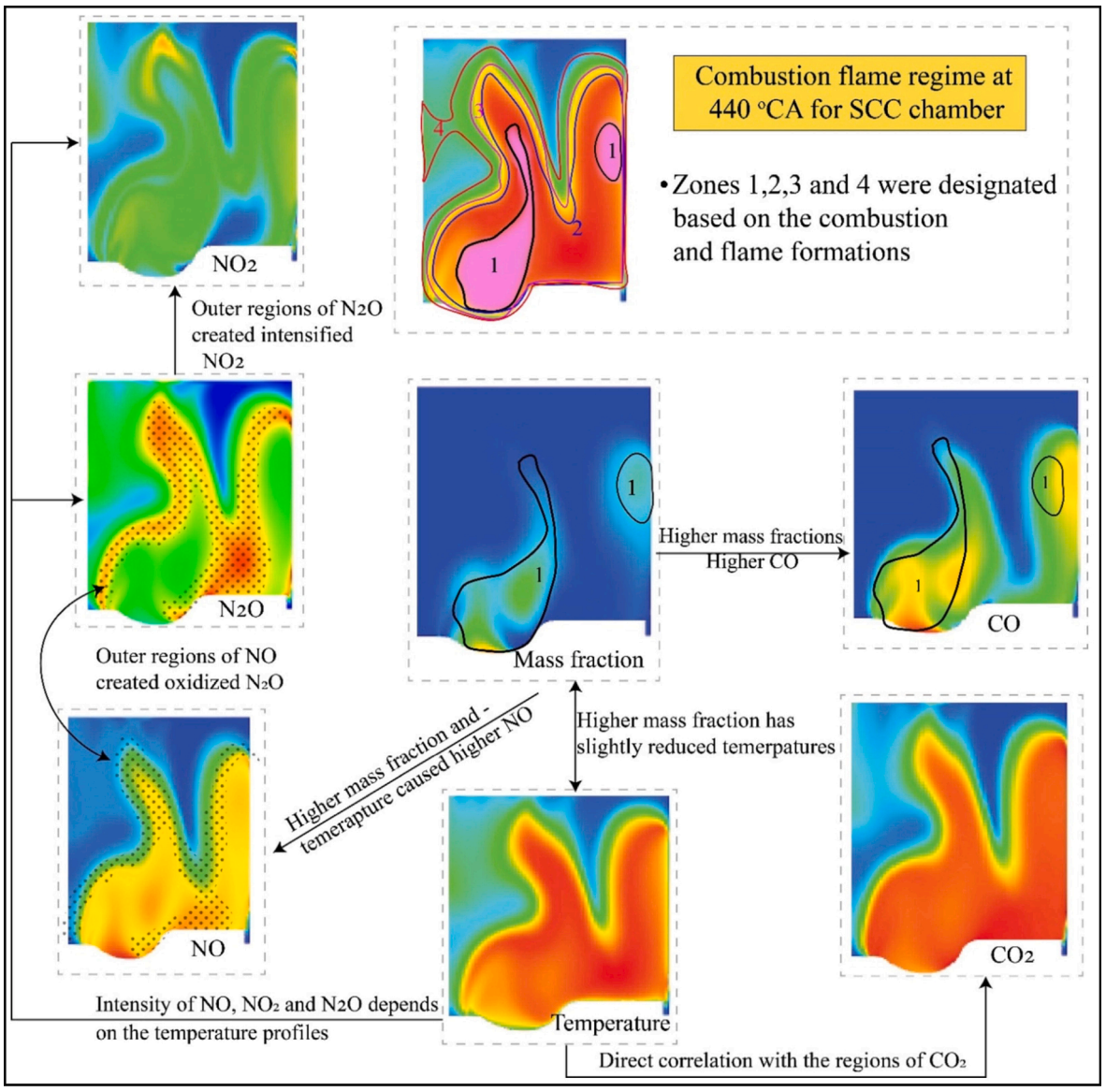


**Fig. 16.** Comparison of combustion parameters with the emission parameters for the SCC chamber at 480 °CA.

secondary oxidation reactions occur, particularly in the cooler outer regions of the combustion chamber, where unburnt fuel and intermediate species can react further [75]. Regions with higher mass fractions of unburnt hydrocarbons and intermediates (like CO) are linked with incomplete combustion areas. The mass fractions of the diesel are due to incomplete combustion, which can be caused by poorer oxidation [76]. The presence of CO and its correlation with mass fractions indicates regions with rich fuel–air mixtures where combustion is incomplete, leading to more CO formation [77,78]. Conversely, regions with adequate oxygen supply and higher temperatures result in more complete combustion, producing $CO_2$ [79]. The oxidation of CO leads to $CO_2$; hence, as presented in Figs. 15 and 16, $CO_2$ has been formed around the surrounding areas of the CO emissions [80].

The combustion in the local regions varies with the bowl profiles. As presented in Figs. 15 and 16, combustion in bowl chambers naturally creates zones with varying air–fuel ratios. This stratification leads to different combustion characteristics across the chamber, influencing temperature and species distribution [81,82]. The fuel mass fraction and temperature contours clearly reveal their nature in terms of emission formation. The amount of oxygen in that particular area, the temperature peak and the temperature gradient found in the first kinetic stage of the combustion process [83]. These aspects trigger higher $NO_x$ emissions, and these actions can be clearly observed in Fig. 14. Also, it is noticed that peak NO emissions are formed at the fuel mass fraction area. It is due to the rapid burning of mass fractions at high temperatures that led to elevated NO emissions [84]. In contrast, $N_2O$ emissions are formed in the medium-temperature zones around the high-temperature areas. Hence, higher $N_2O$ emissions are noticed in the outer curvature of the temperature and NO zones [85]. Compared to NO and $N_2O$ emissions, $NO_2$ has shown lower concentrations and is distributed along with the NO emissions region [86]. The fuel mass fraction and temperature contours clearly reveal their nature in terms of emission formation. For instance, Guo et al. [87] observed a decrease in $NO_x$ by 17 % with the optimized bowl chambers. Optimizing the bowl geometry could reduce the un-burnt mass fractions and reduce the $NO_x$ emissions.

## 4. Conclusion and Recommendations

The study conducted engine tests to measure performance, emission and in-cylinder combustion parameters at full load conditions. A numerical model was developed for CFD simulation and validated with the experimental data. The study investigated the combustion kinetics and emission formation phenomena for four different combustion chamber geometries. The result revealed that the modifications improved performance and reduced emissions. However, the combustion dynamics inside the cylinder remain unpredictable. The main conclusions are as follows:

1) At 1500 rpm, the engine achieved a BP of 35 kW, BSFC of 0.254 kg/kWh, BMEP of 8.61 bar, and BTE of 33.16 %. Whereas emissions were recorded as 1148 ppm of CO, 11.07 % by volume of $CO_2$, 28 ppm of HC, and 234 ppm of $NO_x$.
1) The chamber modifications have promoted the air–fuel mixtures by avoiding the fuel pockets through enhanced turbulent motions. The swirl and tumble motions suggest that the GCC and SCC showed better in-cylinder fluid motions compared to the standard chamber and BTCC.
2) The temperature and TKE contours are used to successfully demonstrate the initiation and generation of combustion and lead to early premixed combustion. Hence, peak HRR values are noted early for GCC (373 °CA), SCC (369 °CA), and BTCC (367 °CA) compared to FCC (380 °CA).
3) Higher CO emissions are noted in the case of chambers, where the unburnt fuel fractions are formed and lower at high-temperature regions. At 480 °CA, the peak value of CO was decreased for GCC, SCC, and BTCC by 91.57 %, 90 %, and 91.05 %, respectively.
4) NO emissions are directly aligned in the regions where high TKE, temperature, and unburnt mass fraction regions are noticed. At 480 °CA, GCC showed a 1.90 % increase in NO compared to FCC, and on the other hand, GCC showed a 17.35 % and 12.38 % decrease in NO compared to SCC and BTCC, respectively.

The study recommends that among the investigated chambers, GCC showed better combustion results and less $NO_x$. To avoid the fuel impingements on the cylinder head, it is further recommended to increase the depth of the GCC chamber. Furthermore, optimizing the injection nozzle according to the groove location of GCC is strongly recommended, as injection plumes significantly influence combustion dynamics.

## Declaration of competing interest

The authors declare that they have no known competing financial interests or personal relationships that could have appeared to influence the work reported in this paper.

## Data availability

Data will be made available on request.

## References


[1] IEA. *Tracking Clean Energy Progress 2023*. 2023 08/10/2024]; Available from: https://www.iea.org/energy-system/transport.
[2] A.K. Azad, A.T. Doppalapudi, M.M.K. Khan, N.M.S. Hassan, P. Gudimetla, A landscape review on biodiesel combustion strategies to reduce emission, Energy Rep. 9 (2023) 4413–4436.
[3] A.T. Doppalapudi, A.K. Azad, M.M.K. Khan, Combustion chamber modifications to improve diesel engine performance and reduce emissions: a review, Renew. Sustain. Energy Rev. 152 (2021) 111683.
[4] V. Karthickeyan, S. Thiyagarajan, B. Ashok, V. Edwin Geo, A.K. Azad, Experimental investigation of pomegranate oil methyl ester in ceramic coated engine at different operating condition in direct injection diesel engine with energy and exergy analysis, Energ. Conver. Manage. 205 (2020) 112334.
[5] A.T. Doppalapudi, A.K. Azad, M.M.K. Khan, Experimental investigation on diesel engine performance, combustion, and emissions characteristics with Tucuma and Ungurahui biodiesel blends, Fuel 371 (2024) 132161.
[6] M.M. Rahman, M.G. Rasul, N.M.S. Hassan, A.K. Azad, M.N. Uddin, Effect of small proportion of butanol additive on the performance, emission, and combustion of Australian native first- and second-generation biodiesel in a diesel engine, Environ. Sci. Pollut. Res. 24 (28) (2017) 22402–22413.
[7] G.G. Gianetti, T. Lucchini, G. D'Errico, A. Onorati, P. Soltic, Development and validation of a CFD combustion model for natural gas engines operating with different piston bowls, Energies 16 (2023), https://doi.org/10.3390/en16020971.
[8] U.S. Jyothi, K.V.K. Reddy, CFD analysis on particle diameter in hydrogen-enriched diesel engine for different piston bowl geometries, Int. J. Ambient Energy 43 (1) (2022) 1661–1670.
[9] N. Seelam, S.K. Gugulothu, B. Bhasker, S. Mulugundum, G.R. Sastry, Investigating the role of fuel injection pressure and piston bowl geometries to enhance performance and emission characteristics of hydrogen-enriched diesel/1-pentanol fueled in CRDI diesel engine, Environ. Sci. Pollut. Res. (2022).
[10] F. Millo, A. Piano, S. Roggio, J.V. Pastor, C. Micó, F. Lewiski, F.C. Pesce, A. Vassallo, A. Bianco, Mixture formation and combustion process analysis of an innovative diesel piston bowl design through the synergetic application of numerical and optical techniques, Fuel 309 (2022) 122144.
[11] L. Xu, X.-S. Bai, Y. Li, M. Treacy, C. Li, P. Tunestål, M. Tunér, X. Lu, Effect of piston bowl geometry and compression ratio on in-cylinder combustion and engine performance in a gasoline direct-injection compression ignition engine under different injection conditions, Appl. Energy 280 (2020) 115920.
[12] P. Kumar, A. Rehman, Bio-diesel in homogeneous charge compression ignition (HCCI) combustion, Renew. Sustain. Energy Rev. 56 (2016) 536–550.
[13] H.E. Gulcan, M. Ciniviz, Experimental study on the effect of piston bowl geometry on the combustion performance and pollutant emissions of methane-diesel common rail dual-fuel engine, Fuel 345 (2023) 128175.
[14] V. Gnanamoorthi, N.M. Marudhan, D. Gobalakichenin, Effect of combustion chamber geometry on performance, combustion, and emission of direct injection diesel engine with ethanol-diesel blend, Therm. Sci. 20 (suppl. 4) (2016) 937–946.
[15] S. Jaichandar, K. Annamalai, Influences of re-entrant combustion chamber geometry on the performance of Pongamia biodiesel in a DI diesel engine, Energy 44 (1) (2012) 633–640.
[16] S.K. Nayak, P.C. Mishra, Achieving high performance and low emission in a dual fuel operated engine with varied injection parameters and combustion chamber shapes, Energ. Conver. Manage. 180 (2019) 1–24.
[17] S. Vedharaj, R. Vallinayagam, W.M. Yang, C.G. Saravanan, P.S. Lee, Optimization of combustion bowl geometry for the operation of kapok biodiesel – Diesel blends in a stationary diesel engine, Fuel 139 (2015) 561–567.
[18] B. Dhinesh, M. Annamalai, I.J. Lalvani, K. Annamalai, Studies on the influence of combustion bowl modification for the operation of Cymbopogon flexuosus biofuel based diesel blends in a DI diesel engine, Appl. Therm. Eng. 112 (2017) 627–637.
[19] S. Jaichandar, K. Annamalai, Combined impact of injection pressure and combustion chamber geometry on the performance of a biodiesel fueled diesel engine, Energy 55 (2013) 330–339.
[20] S. Jaichandar, P.S. Kumar, K. Annamalai, Combined effect of injection timing and combustion chamber geometry on the performance of a biodiesel fueled diesel engine, Energy 47 (1) (2012) 388–394.
[21] S. Khan, R. Panua, P.K. Bose, The impact of combustion chamber configuration on combustion and emissions of a single cylinder diesel engine fuelled with soybean methyl ester blends with diesel, Renew. Energy 143 (2019) 335–351.
[22] İ. Temizer, Ö. Cihan, Analysis of different combustion chamber geometries using hydrogen / diesel fuel in a diesel engine, Energy Sources Part A 43 (1) (2021) 17–34.
[23] J.V. Pastor, A. García, C. Micó, F. Lewiski, A. Vassallo, F.C. Pesce, Effect of a novel piston geometry on the combustion process of a light-duty compression ignition engine: an optical analysis, Energy 221 (2021) 119764.
[24] V. Karthickeyan, Effect of combustion chamber bowl geometry modification on engine performance, combustion and emission characteristics of biodiesel fuelled diesel engine with its energy and exergy analysis, Energy 176 (2019) 830–852.
[25] V.R. Mamilla, M. Mallikarjun, G.L.N. Rao, Effect of combustion chamber design on a DI diesel engine fuelled with jatropha methyl esters blends with diesel, Procedia Eng. 64 (2013) 479–490.
[26] V. Kumar, Experimental investigation of piston bowl geometry effects on performance and emissions characteristics of diesel engine at variable injection pressure and timings, Int. J. Ambient Energy 39 (7) (2018) 685–693.
[27] H. Zhou, X. Li, W. Zhao, F. Liu, Effects of separated swirl combustion chamber geometries on the combustion and emission characteristics of DI diesel engines, Fuel 253 (2019) 488–500.
[28] M.A. Hazrat, M.G. Rasul, M. Mofijur, M.M.K. Khan, F. Djavanroodi, A.K. Azad, M. M.K. Bhuiya, A.S. Silitonga, A mini review on the cold flow properties of biodiesel and its blends, Front. Energy Res. 8 (2020).
[29] D.K. Dasrath, R. Biwalkar, S. Singh, W.F. Northrop, Bowl piston geometry as an alternative to enlarged crevice pistons for rapid compression machines, Proc. Combust. Inst. 38 (4) (2021) 5723–5731.
[30] T.Q. Nguyen, A.y. Dunin, Investigation into the impact of piston bowl size on diesel engine characteristics with changes in fuel injection pressure and boost pressure, Appl. Sci. 14 (2024), https://doi.org/10.3390/app14104334.
[31] H. Sapra, R. Hessel, N. Miganakallu, J. Stafford, E. Amezcua, D. Rothamer, K. Kim, C.M. Kweon, S. Kokjohn, Computational fluid dynamics and Machine learning-based Piston-Bowl optimization for Energy-Assisted compression ignition of low cetane number sustainable aviation fuel blends, Energ. Conver. Manage. 300 (2024) 117929.

[32] V. V, M. J.M, Effect of baffles in the combustion chamber of a gasoline direct injection engine – a computational fluid dynamics analysis, Energy 292 (2024) 130342.

[33] A. Taibani, M. Visaria, S. Krishnan, A combined Combustion-Conjugate heat transfer analysis for Design of partially insulated pistons, Appl. Therm. Eng. 208 (2022) 118210.

[34] G. Xu, A. García, M. Jia, J. Monsalve-Serrano, Computational optimization of the piston bowl geometry for the different combustion regimes of the dual-mode dual-fuel (DMDF) concept through an improved genetic algorithm, Energ. Conver. Manage. 246 (2021) 114658.

[35] A.T. Doppalapudi, A.K. Azad, M.M.K. Khan, Exergy, energy, performance, and combustion analysis for biodiesel NOx reduction using new blends with alcohol, nanoparticle, and essential oil, J. Clean. Prod. 467 (2024) 142968.

[36] Kubota-V3300, *Kubota Workshop manual V3300*. 2004.

[37] A.T. Doppalapudi, A.K. Azad, M.M. Khan, Analysis of improved in-cylinder combustion characteristics with chamber modifications of the diesel engine, Energies 16 (2023), https://doi.org/10.3390/en16062586.

[38] A.K. Azad, M.G. Rasul, M.M.K. Khan, S.C. Sharma, M.M.K. Bhuiya, Recent development of biodiesel combustion strategies and modelling for compression ignition engines, Renew. Sustain. Energy Rev. 56 (2016) 1068–1086.

[39] Azad, A.K., P. Halder, K. Nanthagopal, and B. Ashok, *Chapter 13 - Investigation of diesel engine in cylinder flow phenomena using CFD cold flow simulation*, in *Advanced Biofuels*, A.K. Azad and M. Rasul, Editors. 2019, Woodhead Publishing. p. 329-336.

[40] manual, A., *Ansys Forte theory manual.* 2020 R2.

[41] V. Yakhot, S.A. Orszag, Renormalization group analysis of turbulence. I. Basic theory, J. Sci. Comput. 1 (1) (1986) 3–51.

[42] inc, A., *ANSYS Fluent User's Guide*. 2021.

[43] V. Yakhot, S.A. Orszag, S. Thangam, T. Gatski, C. Speziale, Development of turbulence models for shear flows by a double expansion technique, Phys. Fluids A 4 (7) (1992) 1510–1520.

[44] V. Chintala, K.A. Subramanian, CFD analysis on effect of localized in-cylinder temperature on nitric oxide (NO) emission in a compression ignition engine under hydrogen-diesel dual-fuel mode, Energy 116 (2016) 470–488.

[45] K. Lejda, P. Woś, Simulation and experimental coupled research of rate of heat release in DI diesel engine for various injection strategies, Combust. Engines 132 (1) (2008) 17–24, https://doi.org/10.19206/CE-117279.

[46] J. Benajes, J.V. Pastor, A. García, J. Monsalve-Serrano, An experimental investigation on the influence of piston bowl geometry on RCCI performance and emissions in a heavy-duty engine, Energ. Conver. Manage. 103 (2015) 1019–1030.

[47] L. Ranganatha Swamy, T. Chandrashekar, N. Banapurmath, P. Nashipudi, Effect of injection timing, combustion chamber shapes and nozzle geometry on the diesel engine performance, Universal Journal of Petroleum Sciences 2 (2014) 74–95.

[48] Guo, H. and B. Liko, Injector Tip Temperature and Combustion Performance of a Natural Gas-Diesel Dual Fuel Engine at Medium and High Load Conditions. 2018. V001T03A021.

[49] K. Rajan, K.R. Senthil Kumar, Experimental study on diesel engine working characteristics using yellow oleander biodiesel with the effect of different injection timings, Energy Sources Part A 46 (1) (2024) 4939–4952.

[50] A.K. Azad, P. Halder, Q. Wu, M.G. Rasul, N.M.S. Hassan, V. Karthickeyan, Experimental investigation of ternary biodiesel blends combustion in a diesel engine to reduce emissions, Energy Convers. Manage.: X 20 (2023) 100499.

[51] K. Ali, C. Kim, Y. Lee, S. Oh, K. Kim, A comparative numerical study of the combustion performance of the syngas-fueled HCCI engine using a toroidal piston, square bowl piston, and flat piston shape at different loads, J. Energy Res. Technol. 143 (7) (2021) 072305.

[52] B. Harshavardhan, J. Mallikarjuna, Effect of piston shape on in-cylinder flows and air–fuel interaction in a direct injection spark ignition engine–A CFD analysis, Energy 81 (2015) 361–372.

[53] H.-M. Li, G.-X. Li, Y.-H. Jiang, L. Li, F.-S. Li, Flame stability and propagation characteristics for combustion in air for an equimolar mixture of hydrogen and carbon monoxide in turbulent conditions, Energy 157 (2018) 76–86.

[54] Wu, C., K. Deng, and Z. Wang, *The effect of combustion chamber shape on cylinder flow and lean combustion process in a large bore spark-ignition CNG engine.* journal of the energy institute, 2016. **89**(2): p. 240-247.

[55] P. Yang, Y. Luo, S. Jin, Z. Zi, B. Wu, Study on the effect of turbulent jet combustion chamber on combustion characteristics at different ammonia energy ratio and optimization of an ammonia-diesel dual-fuel engine, J. Energy Inst. 112 (2024) 101431.

[56] S. Tanov, L. Pachano, Ö. Andersson, Z. Wang, M. Richter, J.V. Pastor, J.M. García-Oliver, A. García, Influence of spatial and temporal distribution of Turbulent Kinetic Energy on heat transfer coefficient in a light duty CI engine operating with Partially Premixed Combustion, Appl. Therm. Eng. 129 (2018) 31–40.

[57] P. Sandeep Varma, M. Mittal, Investigations with bowl-in-piston (CI type) and flat-piston (SI type) geometries to study the engine characteristics of a CI engine retrofitted for SI operation with CNG fuel, Energ. Conver. Manage. 301 (2024) 118083.

[58] J. Yadav, P. Venkatesh, S. Pischinger, Application of micro-genetic algorithms to optimize piston bowl geometries for heavy-duty engines running on diesel and 1-Octanol fuels, Appl. Therm. Eng. 226 (2023) 120236.

[59] D. Zhao, Y. Pei, Y. An, J. Hu, Z. Zhang, J. Sun, D. Gao, Evaluation of the turbulent hot jet flame characteristics for achieving high thermal efficiency of hybrid engine, Appl. Therm. Eng. 236 (2024) 121611.

[60] M. Channappagoudra, K. Ramesh, G. Manavendra, Comparative study of standard engine and modified engine with different piston bowl geometries operated with B20 fuel blend, Renew. Energy 133 (2019) 216–232.

[61] B. Harshavardhan, J. Mallikarjuna, CFD analysis of in-cylinder flow and air-fuel interaction on different combustion chamber geometry in DISI engine, Int. J. Theor. Appl. Res. Mech. Eng 2 (3) (2013) 104–108.

[62] B.M. Krishna, J. Mallikarjuna, Tumble flow analysis in an unfired engine using particle image velocimetry, International Journal of Mechanical and Mechatronics Engineering 3 (6) (2009) 706–711.

[63] S. Lee, S. Park, Optimization of the piston bowl geometry and the operating conditions of a gasoline-diesel dual-fuel engine based on a compression ignition engine, Energy 121 (2017) 433–448.

[64] M. Tang, Y. Pei, H. Guo, Y. Zhang, R. Torelli, D. Probst, C. Fütterer, M. Traver, Piston bowl geometry effects on gasoline compression ignition in a heavy-duty diesel engine, J. Energy Res. Technol. 143 (6) (2021) 062309.

[65] H. Yu, X. Liang, G. Shu, Numerical study of the early injection parameters on wall wetting characteristics of an HCCI diesel engine using early injection strategy, Int. J. Automot. Technol. 18 (5) (2017) 759–768.

[66] S. Lahane, K. Subramanian, Impact of nozzle holes configuration on fuel spray, wall impingement and NOx emission of a diesel engine for biodiesel–diesel blend (B20), Appl. Therm. Eng. 64 (1–2) (2014) 307–314.

[67] T. Kitamura, T. Ito, J. Senda, H. Fujimoto, Mechanism of smokeless diesel combustion with oxygenated fuels based on the dependence of the equivalence ration and temperature on soot particle formation, Int. J. Engine Res. 3 (4) (2002) 223–248.

[68] A. Calam, H. Solmaz, A. Uyumaz, S. Polat, E. Yilmaz, Y. İçingür, Investigation of usability of the fusel oil in a single cylinder spark ignition engine, J. Energy Inst. 88 (3) (2015) 258–265.

[69] A.V. Prabhu, A. Avinash, K. Brindhadevi, A. Pugazhendhi, Performance and emission evaluation of dual fuel CI engine using preheated biogas-air mixture, Sci. Total Environ. 754 (2021) 142389.

[70] M. Channappagoudra, K. Ramesh, G. Manavendra, Effect of piston bowl geometry on diesel engine performance operated with dairy scum biodiesel, Int. J. Ambient Energy 41 (14) (2020) 1628–1638.

[71] V.C. Pham, J.K. Kim, W.-J. Lee, S.-J. Choe, V.V. Le, J.-h. Choi, Effects of piston bowl geometry on combustion and emissions of a four-stroke heavy-duty diesel marine engine, Appl. Sci. 12 (2022), https://doi.org/10.3390/app122413012.

[72] N.K.F. Al-Abboodi, The combined effect of the piston bowl geometry and injection fuel pressure on the compression ignition engine characteristics, CFD Lett. 14 (8) (2022) 43–62.

[73] J. Duan, F. liu, Z. Yang, B. Sun, W. Chen, L. Wang, Study on the NOx emissions mechanism of an HICE under high load, Int. J. Hydrogen Energy 42 (34) (2017) 22027–22035.

[74] A.T. Doppalapudi, A.K. Azad, M.M.K. Khan, Advanced strategies to reduce harmful nitrogen-oxide emissions from biodiesel fueled engine, Renew. Sustain. Energy Rev. 174 (2023) 113123.

[75] H. Zhang, H. Qin, X. Wang, J. Liu, J. Liu, X. Jiang, Mechanisms of the N2O formation and decomposition over coal char surface, Combust. Flame 238 (2022) 111923.

[76] J. Hirkude, A.S. Padalkar, Experimental investigation of the effect of compression ratio on performance and emissions of CI engine operated with waste fried oil methyl ester blend, Fuel Process. Technol. 128 (2014) 367–375.

[77] Adhiseshan, J.S., S. Abirama Sundaram, and L. Saravanakumar, *Experimental investigations of a single cylinder four stroke diesel engine using modified piston bowl fuelled with Jojoba biodiesel blend.* Materials Today: Proceedings, 2021. **46**: p. 9844-9849.

[78] R.C. Costa, J.R. Sodré, Compression ratio effects on an ethanol/gasoline fuelled engine performance, Appl. Therm. Eng. 31 (2) (2011) 278–283.

[79] K. Shojae, M. Mahdavian, E. Baghshani, Investigation of piston bowl geometry, injection timing, and EGR mass fraction to improve the performance of ISM 370 diesel engine, Fuel 324 (2022) 124422.

[80] W. Li, B. Fan, P. Jiang, W. Liu, J. Pan, S. Huo, Y. Wu, Q. Lu, Exploring the coupling mechanism between piston structure and turbulent jet ignition mode in hydrogen mixed natural gas rotary engines, Int. J. Hydrogen Energy 63 (2024) 905–917.

[81] Li, C., L. Xu, X.-S. Bai, P. Tunestal, and M. Tuner, *Effect of Piston Geometry on Stratification Formation in the Transition from HCCI to PPC*. 2018, SAE Technical Paper.

[82] S. Shirvani, S. Shirvani, A.H. Shamekhi, R.D. Reitz, An investigation of the effects of the piston bowl geometries of a heavy-duty engine on performance and emissions using direct dual fuel stratification strategy, and proposing two new piston profiles, SAE Int. J. Engines 13 (3) (2020) 311–332.

[83] A.O. Hasan, A.I. Osman, A.a.H. Al-Muhtaseb, H. Al-Rawashdeh, A. Abu-jrai, R. Ahmad, M.R. Gomaa, T.J. Deka, D.W. Rooney, An experimental study of engine characteristics and tailpipe emissions from modern DI diesel engine fuelled with methanol/diesel blends, Fuel Process. Technol. 220 (2021) 106901.

[84] S.R. Turns, F.H. Myhr, R.V. Bandaru, E.R. Maund, Oxides of nitrogen emissions from turbulent jet flames: Part II—Fuel dilution and partial premixing effects, Combust. Flame 93 (3) (1993) 255–269.

[85] A.T. Doppalapudi, A.K. Azad, Advanced numerical analysis of in-cylinder combustion and NOx formation using different chamber geometries, Fire 7 (2024), https://doi.org/10.3390/fire7020035.

[86] R. Alvarez, M. Weilenmann, J.-Y. Favez, Evidence of increased mass fraction of NO2 within real-world NOx emissions of modern light vehicles — derived from a reliable online measuring method, Atmos. Environ. 42 (19) (2008) 4699–4707.

[87] Guo, Z., X. He, Y. Pei, C.-T. Chang, P. Wang, X. Sun, B. Wang, S. Liu, Z. Wang, and S. Shuai, *Optimization of piston bowl geometry for a low emission heavy-duty diesel engine*. 2020, SAE Technical Paper.